J. Fluid Mech. (2008), *vol.* 605, *pp.* 19–45.
doi:10.1017/S0022112008001377 Printed in the United Kingdom

Nonlinear mode selection in a model of trailing line vortices

MALEK ABID

IRPHE - UMR 6594, Technopôle de Château-Gombert, 49 rue Joliot Curie – BP 146, 13384 Marseille Cedex 13, France

(Received 12 July 2007 and in revised form 27 February 2008)

Nonlinear mode selection, from initial random Gaussian field perturbations, in a model of trailing line vortices (swirling jets), in the breakdown regime, is addressed by direct numerical simulations with a Reynolds number equal to 1000. A new concept of mode activity in the nonlinear evolution is introduced. The selected modes, according to their activities, are reported and related to strain eigenvectors (with maximum eigenvalues) of the basic flow corresponding to the trailing line vortex under consideration. The selected modes are also related to results from the linear eigenmode (exponential growth) instability theory using the concept of dispersion relation envelope. It is found that the global mode hypothesis of the linear eigenmode theory is violated near the flow axis when the swirl number increases. However, far from the flow axis the linear eigenmode theory is in good agreement with the nonlinear evolution in the breakdown regime. The discrepancy between the nonlinear evolution and the linear eigenmode theory is related to the transient growth of optimal perturbations resulting from the non-normality of the linearized Navier–Stokes equations about shear flows. A clear distinction between an eigenmode, an optimal perturbation (non-modal) and a direct numerical simulation (DNS) mode is made. It is shown that the algebraic (transient) growth contributions from the inviscid continuous spectrum could trigger nonlinearities near the flow axis. The DNS mode selected in the nonlinear regime coincides with the long-wave eigenmode benefiting from the algebraic growth in the linear regime. This eigenmode is different from the short-wave eigenmode with the absolute maximum exponential growth. Although it is promoted by transients, in the linear regime, the long-wave component is selected nonlinearly.

1. Introduction

Trailing line vortices belong to the large class of swirling flows. These flows are encountered in many situations such as behind airplanes, in turbulence, in rotating cavities, in turbomachinery and in combustion. The Batchelor vortex is a model of trailing line vortices which was the subject of intensive fundamental work, in the last few decades. This issue is pursued in the present work.

Batchelor (1964) gives a similarity solution for the flow in a trailing vortex far downstream from one side of a wing. A characteristic feature of this solution is the existence of strong axial currents near the axis of symmetry. Therefore, the flow is characterized by a swirl parameter, q, involving the ratio of the magnitude of the maximum swirl velocity to that of the maximum axial velocity. In fact, a simplified version of the Batchelor vortex, known as the q vortex, will be studied here.

In the literature, three kinds of instability of this swirling flow have been documented.

(*a*) Inviscid eigenmode instability (exponential instability): the exponential growth rate increases to a finite value as $Re \to \infty$.

(*b*) Viscous eigenmode instability: the exponential growth rate decreases to zero as $Re \to \infty$.

(*c*) Optimal perturbation instability: the growth rate is algebraic and transient.

The inviscid eigenmode instability, with respect to infinitesimal non-axisymmetric (helical) disturbances, was studied by Lessen, Singh & Paillet (1974), Leibovich & Stewartson (1983) and others. A sufficient condition for instability was given: $|q| < 2.31$, in the work by Stewartson & Brown (1985), and it was confirmed by Heaton (2007) who also found that the inviscid instability becomes weak for $|q| > 1.6$.

Viscous eigenmode instability was carried out by Khorrami (1991), Duck & Khorrami (1992) and Mayer & Powell (1992). The destabilizing role of viscous forces, at large Reynolds numbers, has been shown to produce two types of viscous instability normal modes: axisymmetric and asymmetric. Both disturbances are long-wave instabilities with maximum growth rates being orders of magnitude smaller than the inviscid normal modes. Unstable viscous eigenmodes are also present in the stable inviscid range: $|q| > 2.31$, as discovered by Fabre & Jacquin (2004) and studied asymptotically for large Reynolds numbers in Le Dizès & Fabre (2007). These eigenmodes also have growth rates orders of magnitude smaller than the inviscid ones (for $|q| < 2$) and are not considered in the present work.

Optimal perturbations are remnants of the continuous spectrum and are, thus, inviscid in nature. They are characterized by an algebraic growth and are weaker than the eigenmodes. They were discovered by Heaton & Peake (2006) who found that they can affect vortices when $Re = \infty$. When $Re < \infty$, the algebraic growth is asymptotically dumped and becomes a transient growth. Transient effects are present for all finite values of q. For $q \to \infty$ (a Lamb–Oseen vortex), the flow is exponentially stable and the transient effects are also present, as shown in Antkowiak & Brancher (2004) and in Pradeep & Hussain (2006).

Direct numerical simulation of the nonlinear evolution of the Batchelor trailing q vortex, when perturbed, was addressed by Abid & Brachet (1998) from a temporal point of view. It was shown that, globally, the vortex is submitted to two phases: a breakdown phase, where the vortex changes drastically from its initial shape, followed by a relaminarization phase. The transition between the two phases is marked by a maximum energy transfer from the axial velocity to the radial one, and no stagnation-point flow is needed to promote breakdown. Delbende & Rossi (2005) studied the nonlinear evolution of two types of initial perturbation: a single unstable eigenmode, with given azimuthal symmetry; and white noise. They found similar trends for both perturbations, but no systematic quantitative study was given for the white-noise perturbation case. The objective of this paper is to complete the work by Delbende & Rossi and to address more specifically the nonlinear evolution of the Batchelor trailing q vortex when perturbed with a weak Gaussian random field.

Spatial direct numerical simulations of swirling jets were addressed by Ruith *et al.* (2003) and Herrada & Fernandez-Feria (2006). They are beyond the scope of the present work which will focus on the evolution in a temporal framework exclusively. The same remark is valid for linear spatial instabilities of swirling flows studied in Olendraru *et al.* (1996), Delbende, Chomaz & Huerre (1998) and Gallaire & Chomaz (2003).

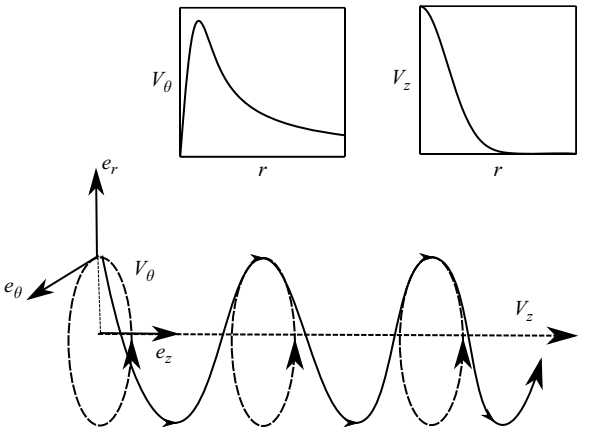

FIGURE 1. Helical particle path in the Batchelor q vortex. The insets show the radial dependence of the azimuthal velocity, V_θ, and the axial one, V_z, at a given time.

The paper is organized as follows. The Batchelor q vortex flow is briefly recalled in § 2. Then, results from the perturbation energy equation are presented in § 3 followed by results from the linear instability theory in § 4. The nonlinear mode selection is studied in § 5, and § 6 is devoted to a summary of results and conclusion. Finally, details of the numerical method are given in the Appendix.

2. The Batchelor q vortex

In a cylindrical frame, $(\boldsymbol{e}_r, \boldsymbol{e}_\theta, \boldsymbol{e}_z)$, the Batchelor q vortex (BqV) is the flow with axial (jet) and azimuthal (vortex) components of the velocity field: $\boldsymbol{V}(\boldsymbol{x}, t) = (0, V_\theta, V_z)$ with

$$V_\theta \equiv V = qW_0 \frac{1 - \exp(-(r/a(t))^2)}{(r/a_0)}, \quad V_z \equiv W = \frac{W_0}{(a/a_0)^2} \exp(-(r/a(t))^2), \tag{2.1}$$

where q is the swirl intensity, $a(t) = \sqrt{a_0^2 + 4\nu t}$ is the vortex/jet core radius and ν is the kinematic viscosity. This flow is an exact solution of the incompressible and constant (unit) density Navier–Stokes equations (NSE) with the pressure field given by $\mathrm{d}P/\mathrm{d}r = V_\theta^2/r$. It is characterized by helical paths of its fluid particles (figure 1). Therefore, patterns with helical symmetry are good candidates for describing the BqV instability.

Unless otherwise stated, a cylindrical frame is used. The initial core radius, a_0, is taken as a unit length, W_0 as a unit velocity and a_0/W_0 as a unit time. Thus, all the physical variables are made non-dimensional using these characteristic length and velocity scales and the Reynolds number is $Re = W_0 a_0/\nu$.

Delbende & Rossi (2005) showed that three values of q are of interest in the ('strong') unstable range $|q| \lesssim 1.6$. For $|q| \simeq 0.4$, the vortex breaks in an array of dipoles. For an intermediate value, $|q| \simeq 0.8$, the vortex breaks in an array of equal sign vortices and for $|q| \simeq 1$ the relaminarization of the vortex is accelerated by differential rotation and viscous effects. Based on these results, three different values of q are considered herein: $-0.4, -0.8$ and -1. The Reynolds number is fixed at $Re = 1000$. This value is the same as used by Delbende & Rossi in their study of the Batchelor q vortex. It is large enough to promote instabilities of the basic flow by nonlinearities and is a reasonable one for carrying out direct numerical simulations,

of the fully nonlinear Navier–Stokes equations, in an acceptable human time. As in the present work, viscous eigenmode instabilities are not considered, that value will not be varied.

3. Results from the perturbation energy equation

As shown in Landau & Lifshitz (1987), a perturbation velocity field $\boldsymbol{v}(\boldsymbol{x}, t)$ superposed to a basic flow $\boldsymbol{V}(\boldsymbol{x}, t)$ (solution of NSE) satisfies the following energy budget equation:

$$\frac{\mathrm{d}E[\boldsymbol{v}]}{\mathrm{d}t} = -\int_{\mathfrak{D}} \mathrm{d}\boldsymbol{x}\, \boldsymbol{v}\cdot\boldsymbol{S}[\boldsymbol{V}]\cdot\boldsymbol{v} - \nu\int_{\mathfrak{D}} \mathrm{d}\boldsymbol{x}\, \left(\frac{\partial \mathrm{v}_i}{\partial x_j}\right)^2, \tag{3.1}$$

assuming only that the disturbance is periodic. Here, $E[\boldsymbol{v}]$ is the total kinetic energy of the perturbation in the fluid domain $\mathfrak{D}$:

$$E[\boldsymbol{v}] = \int_{\mathfrak{D}} \mathrm{d}\boldsymbol{x}\, \tfrac{1}{2}\boldsymbol{v}^2, \tag{3.2}$$

$\boldsymbol{S}[\boldsymbol{V}]$ is the rate-of-strain tensor of the basic flow:

$$\boldsymbol{S}[\boldsymbol{V}] = \tfrac{1}{2}(\nabla\boldsymbol{V} + \nabla\boldsymbol{V}^T), \tag{3.3}$$

T is the transpose of a tensor and v_i are the components of $\boldsymbol{v}$ in a Cartesian coordinate system. In the last term of (3.1), the summation over repeated indices is assumed.

Note that (3.1) is obtained from the exact nonlinear NSE, whatever the initial perturbation amplitude is infinitesimal or finite. Note also that the last term of (3.1) is always negative, showing the damping effect of viscosity in general. Therefore, in the inviscid limit, the local growth rate of the perturbation, $\sigma_l(\boldsymbol{x}, t) = (\mathrm{d}(\boldsymbol{v}^2)/\mathrm{d}t)/2\boldsymbol{v}^2$, is bounded from above by the maximum eigenvalue, λ, of $\boldsymbol{S}[\boldsymbol{V}]$, which is also an upper bound of the local energy transfer from the basic flow to the perturbation.

In the BqV case,

$$\boldsymbol{S}[\boldsymbol{V}] = \frac{1}{2}\begin{bmatrix} 0 & r\mathrm{D}\Omega & \mathrm{D}W \\ r\mathrm{D}\Omega & 0 & 0 \\ \mathrm{D}W & 0 & 0 \end{bmatrix}, \tag{3.4}$$

$$\lambda = \tfrac{1}{2}\sqrt{(r\mathrm{D}\Omega)^2 + (\mathrm{D}W)^2}, \tag{3.5}$$

corresponding to the eigenvector:

$$\boldsymbol{e}(\lambda) = \left(\frac{2\lambda}{\mathrm{D}W}, \frac{r\mathrm{D}\Omega}{\mathrm{D}W}, 1\right). \tag{3.6}$$

In these equations, $\mathrm{D} \equiv \mathrm{d}/\mathrm{d}r$ is the differentiation with respect to r and $\Omega \equiv V/r$ is the local angular velocity. The eigen vector $\boldsymbol{e}(\lambda)$ defines a privileged direction in the plane (θ, z): $\boldsymbol{e}(\lambda) - (\boldsymbol{e}(\lambda)\cdot\boldsymbol{e}_r)\boldsymbol{e}_r$ with an angle Φ given by:

$$\tan(\Phi) = \frac{1}{r}\frac{\mathrm{d}z}{\mathrm{d}\theta} = \frac{1}{r}\frac{\mathrm{D}W}{\mathrm{D}\Omega}, \tag{3.7}$$

whose signification will be given in the following section.

For the three values of q: $-(0.4, 0.8, 1)$, λ is plotted as a function of r in figure 2. Clearly, the local growth rate cannot exceed $(0.44, 0.46, 0.47)$, respectively. Furthermore, the maximum energy transfer from the basic BqV flow to the perturbation

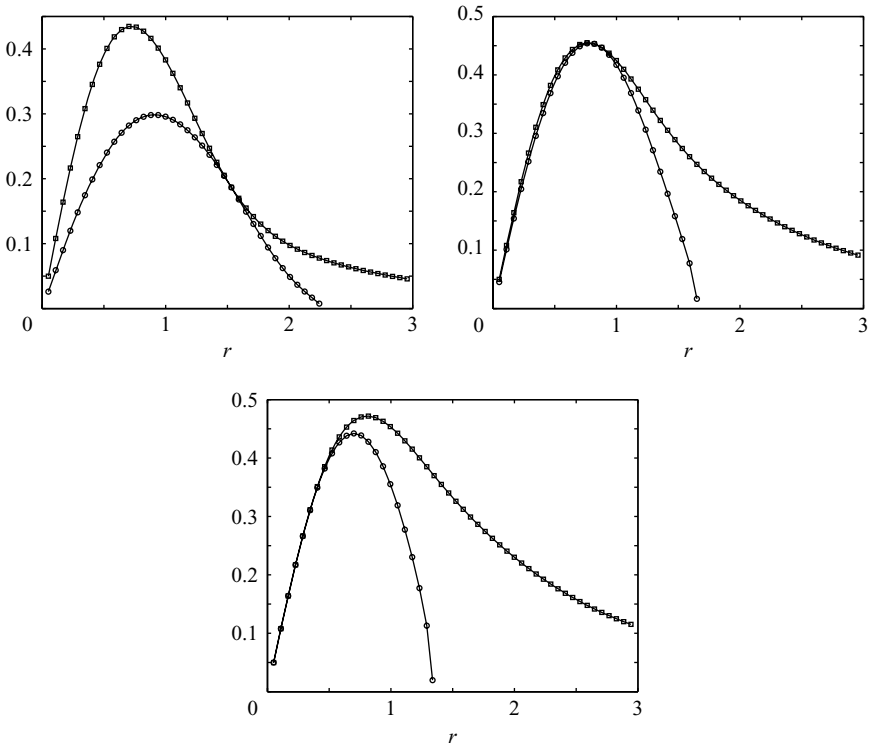

FIGURE 2. Plots of the local growth rate σ_l (○) and the maximum strain rate λ (□) versus r, for (*a*) $q = 0.4$, (*b*) -0.8, (*c*) -1.0.

occurs near the vortex core radius $r = 1$; more precisely: $r \equiv r_\lambda = (0.72, 0.77, 0.81)$ (see figure 2). At those values of r, $\Phi \equiv \Phi_\lambda = -(0.89, 0.77, 0.70)(\pi/2)$.

4. Linear instability results

4.1. *Eigenmodes and optimal perturbations*

After a projection onto the space of divergence-free velocities, the linearized Navier–Stokes equations, for a perturbation velocity $\boldsymbol{v}$ about a basic flow $\boldsymbol{V}$ (here the Batchelor q vortex), could be written as the following initial-value problem for the perturbation:

$$\frac{\partial \boldsymbol{v}}{\partial t} = -\mathrm{i}\mathbb{L}\boldsymbol{v}, \tag{4.1}$$

where $-\mathrm{i}\mathbb{L}\boldsymbol{v} = \mathbb{P}(-\boldsymbol{v}\cdot\nabla\boldsymbol{V} - \boldsymbol{V}\cdot\nabla\boldsymbol{v} + \nu\Delta\boldsymbol{v})$ and $\mathbb{P}$ is the projector onto the divergence-free velocity space.

Formally, using the exponential of an operator, the solution of this linear initial-value problem is:

$$\boldsymbol{v}(\boldsymbol{x}, t) = \mathrm{e}^{-\mathrm{i}\mathbb{L}t}\boldsymbol{v}(\boldsymbol{x}, 0). \tag{4.2}$$

Generally, the linear operator $\mathbb{L}$ is non-normal (with respect to the inner product, $\langle ., . \rangle$, in the $L^2(\mathfrak{D})$ Hilbert space) for shear flows, i.e. it does not commute with its adjoint and its eigenfunctions are not orthogonal. Therefore, two kinds of solution must be distinguished (Butler & Farrell 1992; Trefethen *et al.* 1993; Schmid & Henningson 2001; Schmid 2007): the eigenmodes (characterized by an exponential

growth or decay) and the optimal perturbations (characterized by a possible algebraic growth when eigenmodes decay).

Eigenmodes are the solutions of (4.1) having the form (separation of space and time variables):

$$\boldsymbol{v}(\boldsymbol{x}, t) = \hat{\boldsymbol{v}}(\boldsymbol{x})\mathrm{e}^{-\mathrm{i}\omega t}, \tag{4.3}$$

where $\omega = \omega_r + \mathrm{i}\sigma$ is a complex number to be found. Therefore, eigenmodes are solutions of the following differential eigenvalue problem:

$$\mathbb{L}\hat{\boldsymbol{v}} = \omega\hat{\boldsymbol{v}}. \tag{4.4}$$

In general, the spectrum of $\mathbb{L}$ consists of both a discrete, $(\omega_i, i \in \mathbb{N})$, and a continuous, $(\omega(s), s \in \mathbb{R}^+)$, parts. The completeness of the corresponding set of eigenfunctions, in general, is an open question and to the best of my knowledge there is no general results on the spectral theory for a continuous linear operator $\mathbb{L}$. Nevertheless, if the set of eigenfunctions is complete, an arbitrary disturbance $\boldsymbol{v}$ could be expanded as follows:

$$\boldsymbol{v}(\boldsymbol{x}, t) = \sum_{i\in\mathbb{N}} \kappa_i(t)\hat{\boldsymbol{v}}_i(\boldsymbol{x}) + \int_0^\infty \mathrm{d}s\, \kappa(t, s)\hat{\boldsymbol{v}}(\boldsymbol{x}; s). \tag{4.5}$$

Optimal perturbations (no separation of variables) are those initial perturbations $\boldsymbol{v}_0 \equiv \boldsymbol{v}(\boldsymbol{x}, 0)$ that maximize the energy gain at a given time. They are solutions of the following optimization problem:

$$G(t) \equiv \max_{\boldsymbol{v}_0\neq\boldsymbol{0}} \frac{E[\boldsymbol{v}]}{E[\boldsymbol{v}_0]} = \max_{\boldsymbol{v}_0\neq\boldsymbol{0}} \frac{||\boldsymbol{v}||^2}{||\boldsymbol{v}_0||^2} = \max_{\boldsymbol{v}_0\neq\boldsymbol{0}} \frac{||\mathrm{e}^{-\mathrm{i}\mathbb{L}t}\boldsymbol{v}_0||^2}{||\boldsymbol{v}_0||^2} = ||\mathrm{e}^{-\mathrm{i}\mathbb{L}t}||^2, \tag{4.6}$$

where $G(t)$ is the maximum possible gain (or amplification) in energy of an initial perturbation at time t.

In practice, a discrete approximation, $\mathbb{L}_N$, of the continuous operator $\mathbb{L}$ is used (N is, for example, the number of grid points or the number of Chebyshev polynomials used in the discretization). A finite number, K, of eigenmodes (corresponding to the first K eigenvalues $\{\omega_k\}$ when arranged in order of decreasing imaginary part) in the discretized version of the spectral expansion (4.5) is also used. The numbers N and K are chosen sufficiently large so that:

$$\mathbb{L} \simeq \mathbb{L}_N, \tag{4.7}$$

$$\boldsymbol{v}(\boldsymbol{x}, t) \simeq \sum_{k=1}^{K} \kappa_k(t)\hat{\boldsymbol{v}}_k(\boldsymbol{x}). \tag{4.8}$$

In what follows, the same symbol will be used for a quantity and its discrete approximation. Following Satish & Henningson (1993) let $\boldsymbol{\kappa}(t) = (\kappa_1(t), \kappa_2(t), \ldots, \kappa_K(t))^T$ denote the vector of the expansion coefficients. By (4.1) and (4.8) we have

$$\boldsymbol{\kappa}(t) = \mathrm{e}^{-\mathrm{i}\Lambda t}\boldsymbol{\kappa}(0), \tag{4.9}$$

where Λ is the diagonal matrix of dimension K with the first K eigenvalues $\{\omega_k\}$ on the diagonal. Therefore, $||\boldsymbol{v}||^2 = \boldsymbol{\kappa}^\star(t)A\boldsymbol{\kappa}(t)$, where $\boldsymbol{\kappa}^\star$ is the conjugate transpose of $\boldsymbol{\kappa}$ and A is the Hermitian and positive definite matrix:

$$A_{i,j} = \langle \hat{\boldsymbol{v}}_i, \hat{\boldsymbol{v}}_j \rangle. \tag{4.10}$$

Therefore A could be expressed, using a Cholesky decomposition, as $A = F^{\star}F$. It follows that

$$||\boldsymbol{v}||^2 = \boldsymbol{\kappa}^{\star}(t)F^{\star}F\boldsymbol{\kappa}(t) = ||F\boldsymbol{\kappa}(t)||_2^2, \tag{4.11}$$

where the subscript 2 denotes the 2-norm (Euclidean norm). Therefore:

$$G(t) = \max_{\boldsymbol{\kappa}(0)\neq\mathbf{0}} \frac{||F\boldsymbol{\kappa}(t)||_2^2}{||F\boldsymbol{\kappa}(0)||_2^2} = \max_{\boldsymbol{\kappa}(0)\neq\mathbf{0}} \frac{||F\mathrm{e}^{-\mathrm{i}\Lambda\mathrm{t}}\boldsymbol{\kappa}(0)||_2^2}{||F\boldsymbol{\kappa}(0)||_2^2} = ||F\mathrm{e}^{-\mathrm{i}\Lambda\mathrm{t}}\mathrm{F}^{-1}||_2^2. \tag{4.12}$$

It follows that upper and lower bounds on the gain, G, are given by

$$\begin{aligned} \mathrm{e}^{\sigma_{max}t} &\leqslant \sqrt{G(t)} \\ &\leqslant ||F||_2||F^{-1}||_2\mathrm{e}^{\sigma_{max}t} = \mathrm{cond(F)}\mathrm{e}^{\sigma_{max}t}. \end{aligned} \tag{4.13}$$

where σ_{max} is the maximum value of σ (the imaginary part of an eigenvalue ω) and cond(F) is the condition number of F.

Obviously, for large times optimal perturbations tend, asymptotically, to the eigenmode with the maximum amplification factor and their growth rate $d\log(\sqrt{G(t)})/dt \sim \sigma_{max}$. Therefore, non-normality have found most of its application for stable flows ($\sigma_{max} < 0$) for which the energy gain is bounded, for all t, and $G_{max} = \max_t G(t) \gg 1$ leading to a significantly transient (short-term) growth. It will be shown in the present work that transient effects still play an important role for an unstable flow, especially in the nonlinear regime, since $\sqrt{G(t)} \geqslant \mathrm{e}^{\sigma_{max}t}$ for $\sigma_{max} > 0$ as well.

Notice that for a normal operator $\mathbb{L}$, the optimal perturbation obtained by (4.6) coincides, at each time, with the eigenmode with the maximum exponential growth rate and $\sqrt{G(t)} = \mathrm{e}^{\sigma_{max}t}$. Indeed, for a normal operator the eigenfunctions are orthogonal. Therefore, $A = I$ (the identity matrix), $F = I$, cond(F) = 1 and the upper and lower bounds on $\sqrt{G(t)}$ coincide. Clearly, cond(F) which is a measure of the non-normality is also a measure of the transient growth that may be substantial when cond(F) $\gg 1$.

When necessary, the energy growth function G will be computed by direct numerical simulations of (4.1) and compared with the results of the optimization problem (4.6), kindly given by C. Heaton. The following subsection is devoted to studying the eigenmodes of the BqV.

4.2. *Time asymptotic growth: eigenmodes*

Because of the helical symmetry of the basic flow, the perturbation velocity, $\tilde{\mathbf{v}}$, and pressure, $\tilde{p}$, solutions of the linearized NSE about $(\boldsymbol{V}, P)$, are assumed to be of the form:

$$(\tilde{\mathbf{v}}, \tilde{p}) = (\tilde{u}, \tilde{v}, \tilde{w}, \tilde{p}) = (u(r), v(r), w(r), p(r))\exp[\mathrm{i}(kz + m\theta - \omega t)], \tag{4.14}$$

where $\omega = \omega_r + \mathrm{i}\sigma$ is a complex number to be found, given the axial, $k \in \mathbb{R}$, and azimuthal, $m \in \mathbb{N}$, wavenumbers. When the global (i.e. the same for all r) growth rate, σ, is positive, the flow is linearly unstable for the pair (m, k). At a fixed value of r, this pair defines in the plane (θ, z) an angle (the helix angle, also the equipahse angle), $\tilde{\Phi}$, given by:

$$\tan(\tilde{\Phi}) = \frac{1}{r}\frac{\mathrm{d}z}{\mathrm{d}\theta} = -\frac{1}{r}\frac{m}{k}. \tag{4.15}$$

Therefore, this family of helices is invariant under the symmetry $(m, k) \rightarrow -(m, k)$. The study may be restricted to values of $k \geqslant 0$. The change of the sign of m will thus change only the sign of the rotation of helices. For a clockwise rotation, $\mathrm{d}z/\mathrm{d}\theta \leqslant 0$

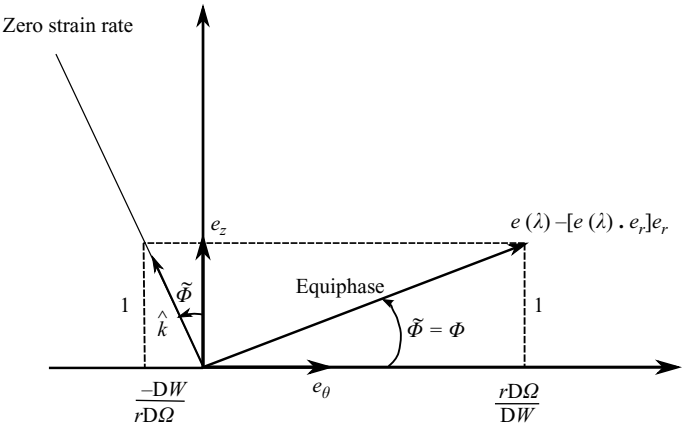

FIGURE 3. Definition of $\tilde{\Phi}$ and its relation with Φ. The vector $\boldsymbol{e}(\lambda)$ is the eigenvector associated with the maximum strain rate eigenvalue, λ, of the basic flow.

and $m \geqslant 0$. This motivated the choice of the negative sign for the swirl parameter (q) in the present study.

4.2.1. *Inviscid results: asymptotic growth*

Using numerical computations, Leibovich & Stewartson (1983) have shown that the BqV flow is stable when $q \lesssim -1.6$ (this value has been updated by Heaton (2007) and actually the flow is stable when $q \lesssim -2.31$). At a fixed value of q in the unstable range they found, using an asymptotic analysis in the limit $m \gg 1$, $k \gg 1$ and $m/k = O(1)$, a class of unstable disturbances whose maximum growth rates increase monotonically with m and are bounded as $m \to \infty$. An element of this class is a helix, concentrated near r, with a local growth rate given by:

$$\sigma_l^2(r) = \frac{2V[rDV - V][V^2/r^2 - (DV)^2 - (DW)^2]}{(rDV - V)^2 + r^2(DW)^2}, \tag{4.16}$$

when the pair (m, k) satisfies:

$$\frac{DW}{D\Omega} = -\frac{m}{k}. \tag{4.17}$$

Asymptotically, this clearly relates $\tilde{\Phi}$ to Φ defined in the previous section: $\tilde{\Phi} = \Phi$ when (4.17) is satisfied. However, for selection, the maximum value of the growth rate is to be considered. Therefore, from all the possible helices (m, k), those having the maximum growth rate, $\max_r \sigma_l(r)$ attained at r_σ, are such that the direction defined by their angle (or simply $-m/(r_\sigma k)$) is aligned with that of the projection of the strain rate eigenvector (with the maximum eigenvalue), in the plane (θ, z), if $r_\sigma \simeq r_\lambda$. This is actually the case (see figure 2). Indeed, for $q = -(0.4, 0.8, 1)$ the maximum local growth rate is attained for $r_\sigma = (0.88, 0.77, 0.70)$. At those values of r, $\tilde{\Phi}_\sigma = -(0.86, 0.77, 0.75)(\pi/2) \simeq \Phi_\lambda$.

Notice that at a fixed r, equation (4.14) defines a unit wave vector: $\widehat{\boldsymbol{k}} = (k\boldsymbol{e}_z + (m/r)\boldsymbol{e}_\theta)/(k^2 + (m/r)^2)$. This vector is orthogonal to the equiphase line, from (4.15), and is aligned with the zero strain rate direction as shown in Stewartson & Leibovich (1987) and illustrated in figure 3. In what follows, r_λ will be used to define helices' angles.

4.2.2. *Viscous results*

After some algebra, the linearized NSE could be written in the following generalized differential eigenvalue problem:

$$\mathscr{A}\begin{bmatrix} u \\ v \\ w \\ p \end{bmatrix} = \omega\mathscr{B}\begin{bmatrix} u \\ v \\ w \\ p \end{bmatrix}, \tag{4.18}$$

where,

$$\mathscr{A} = \begin{bmatrix} \mathrm{i}(m\Omega + kW) - \nu L & -2\Omega + \nu\dfrac{2\mathrm{i}m}{r^2} & 0 & D \\ \Omega + V' - \nu\dfrac{2\mathrm{i}m}{r^2} & \mathrm{i}(m\Omega + kW) - \nu L & 0 & \dfrac{\mathrm{i}m}{r} \\ W' & 0 & \mathrm{i}(m\Omega + kW) - \nu L_w & \mathrm{i}k \\ \mathrm{D} + \dfrac{1}{r} & \dfrac{\mathrm{i}m}{r} & \mathrm{i}k & 0 \end{bmatrix},$$

and

$$\mathscr{B} = \mathrm{i}\begin{bmatrix} 1 & 0 & 0 & 0 \\ 0 & 1 & 0 & 0 \\ 0 & 0 & 1 & 0 \\ 0 & 0 & 0 & 0 \end{bmatrix}, \quad L \equiv \left(\mathrm{D}^2 + \frac{1}{r}\mathrm{D} - k^2 - \frac{m^2+1}{r^2}\right), \quad L_w \equiv L + \frac{1}{r^2}.$$

To be solved, this differential eigenvalue problem is transformed to an algebraic one using spectrally accurate Chebyshev polynomials. To avoid problems with boundary conditions, near $r=0$, the interval $r \in [-\infty, +\infty]$ is used instead of $r \in [0, +\infty]$ (Fabre & Jacquin 2004). The boundary conditions at infinity are vanishing eigenfunctions. Finally, the real axis is mapped to $\xi \in [-1, +1]$ using the function $r = \tan(\pi\xi/2)$. Notice that there is no free parameter in this map. As the viscosity has a damping effect, for the swirl parameter range of interest, the BqV flow at $t=0$ is used for the present linear calculations. The growth rates obtained in this way are upper bounds when the growth rate is considered as a function of viscosity. For the Reynolds number that will be used in the direct numerical simulations, the growth rates will be slightly affected as will be shown in § 5. The overall procedure is checked by reproducing some eigenvalues published in the literature: for example, it is found that $\sigma = 0.24$ when $q = -0.4$, $m = 3$ and $k = 1.09$ which is exactly the value reported in Delbende & Rossi (2005).

Dispersion relations, $\sigma = \sigma(k, m; q)$, are computed for different values of m and q, with $Re = 1000$, using the method described above. From these relations, it is easy to deduce the maximum growth rate envelope: $\sigma_{max}(m) \equiv \max_k \sigma(k, m; q)$ for different values of m at a fixed q. These envelopes are presented in figure 4 and $\sigma_{max}(m)$ is plotted as a function of the wavenumber k_σ, where the maximum is attained, at given m and q. Clearly, perturbations with great values of m are damped and the absolutely most unstable modes are: ($k_\sigma = 0.9, m = 2$) for $q = -0.4$, ($k_\sigma = 2.21, m = 4$) for $q = -0.8$ and ($k_\sigma = 0.24, m = 4$) for $q = -1$. Using r_λ, where the energy transfer from the base flow to perturbations is maximum, the equiphase angle of these global

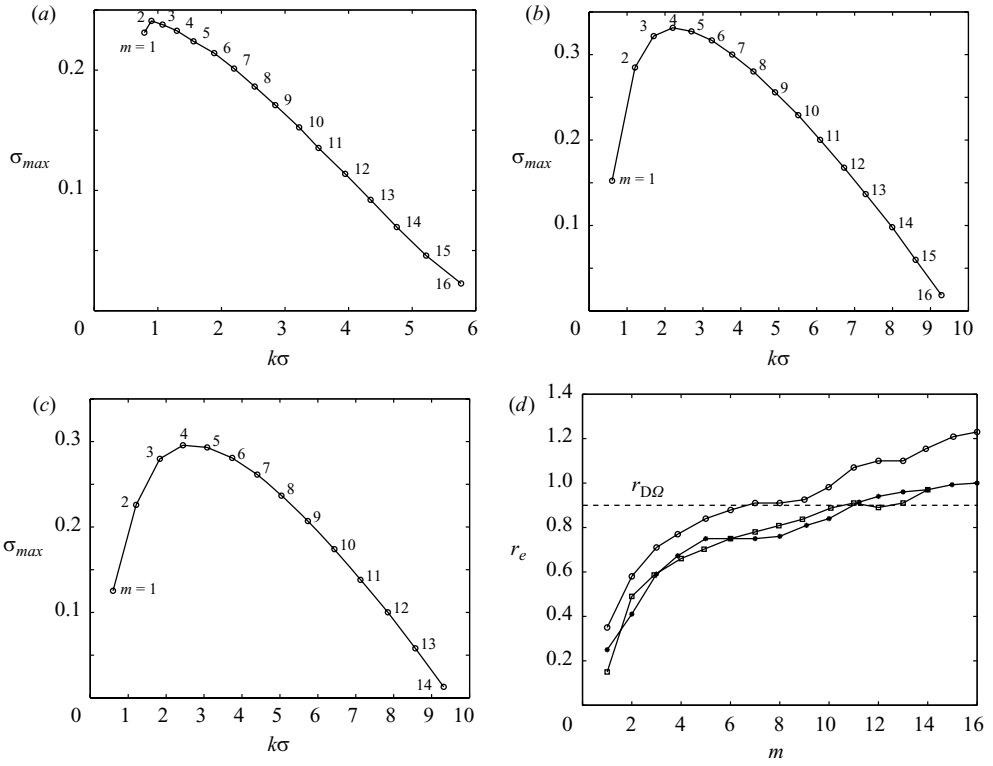

FIGURE 4. The maximum growth rate envelope, $\sigma_{max}(m) = max_k\, \sigma(k, m)$, is plotted against k_σ (where $\sigma_{max}(m)$ is attained) for different values of m and q: (*a*) $q = -0.4$, (*b*) $q = -0.8$ and (*c*) $q = -1$. (*d*) Position of the maximum perturbation energy, r_e, versus m. The value of r where the shear diffusion mechanism is important, $r_{D\Omega}$, is shown using a discontinuous line. ○, $q = -0.4$; ∗, 0.8; □, −1.0.

modes:

$$\tan(\tilde{\Phi}_\lambda^v) = -\frac{1}{r_\lambda}\frac{m}{k_\sigma}, \tag{4.19}$$

is $\tilde{\Phi}_\lambda^v = -(0.8, 0.74, 0.71)(\pi/2)$ for $q = -(0.4, 0.8, 1)$, respectively. In the viscous case, the most unstable eigenmode is approximately aligned with the direction of the maximum strain rate, in the plane (θ, z): $\tilde{\Phi}_\lambda^v \approx \Phi_\lambda$. Notice that this property of near alignment is improved when q increases (figure 5).

A natural question is what happens in a nonlinear evolution issued from a noisy perturbation to the BqV initial condition? Are the linear most unstable eigenmodes selected (eventually solely)? Likewise, what about the non-normality in an exponentially unstable flow? And, finally, what about the tendency of the near alignment? Does it persist? These questions will be addressed in the next section.

Finally, the location of a linear unstable perturbation, belonging to the envelope, could be characterized by the position of the local energy perturbation maximum: $r_e = \arg\max_r(u^2 + v^2 + w^2)/2$. It was checked that this local energy is different from zero in a narrow band around r_e and decreases fast far from it. The different values of r_e obtained in this way are presented in figure 4(*d*). It shows that the eigenmode perturbations with small m are located near the vortex axis, whereas for large m, the eigenmodes are located near the vortex radius $r = 1$. The dumping of eigenmodes

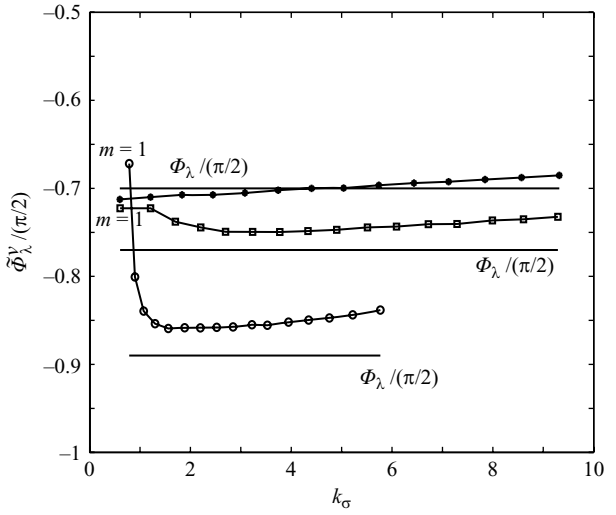

FIGURE 5. Plot of the equiphase angle of the maximum growth rate envelope in the viscous case: $\tilde{\Phi}^v_\lambda$. The angle from the inviscid energy equation, Φ_λ, is also plotted for comparison. Both angles are based on the location, r_λ, of the maximum energy transfer from the base flow to the perturbation. ○, $q=-0.4$, $m\in[1,16]$; □, -0.8, $\in[1,16]$; *, -1.0, $\in[1,14]$.

with large azimuthal wavenumber, m, agrees with the asymptotic theory developed by Stewartson (1982) where a dumping factor of $O(\exp[-\mathrm{Re}^{-1}m^2t])$ for $m\gg 1$ is found.

5. Nonlinear selection

Three-dimensional incompressible and constant (unit) density NSE are solved, using a highly accurate parallel pseudospectral (Fourier) method, in a rectangular domain $\mathfrak{D}=[0,L_x]\times[0,L_y]\times[0,L_z]$. The equations are expressed in rotational formulation:

$$\frac{\partial \boldsymbol{v}}{\partial t}=\boldsymbol{v}\times\boldsymbol{\omega}+\boldsymbol{V}\times\boldsymbol{\omega}+\boldsymbol{v}\times\boldsymbol{\Omega}-\nabla\Pi+\nu\Delta\boldsymbol{v}, \tag{5.1a}$$

$$\Pi=p+\boldsymbol{V}\cdot\boldsymbol{v}+\tfrac{1}{2}\boldsymbol{v}^2, \tag{5.1b}$$

$$\nabla\cdot\boldsymbol{v}=0, \tag{5.1c}$$

$$\boldsymbol{v}(\boldsymbol{x},0)=\boldsymbol{\eta}(\boldsymbol{x}), \tag{5.1d}$$

where p is the pressure, $\boldsymbol{\omega}=\nabla\times\boldsymbol{v}$, $\boldsymbol{\Omega}=\nabla\times\boldsymbol{V}$ and $\boldsymbol{\eta}$ is a Gaussian incompressible random field such that $||\boldsymbol{\eta}(\boldsymbol{x})||_\infty/||\boldsymbol{V}(\boldsymbol{x},0)||_\infty\leqslant 0.01$. The cutoff wavenumbers of the random field are chosen to be $m_c=20$ (at $r=1$) and $k_c=20$. For all the computations, $L_x=L_y=L_z=4\pi$, the spatial resolution is $N_x=N_y=256$, $N_z=64$ giving a maximum resolved azimuthal wavenumber $m_{max}=64$ (at $r=1$) and a maximum resolved longitudinal wavenumber $k_{max}=16$. With the current value of L_x, wavenumbers below $k=0.5$ are not resolved (but $k=0$ is resolved). This is not a severe restriction since the most unstable eigenmodes with the lowest k values are the modes $m=1$ having $k\gtrsim 0.5$, as shown in figure 4 where the growth rate envelopes are reported. Furthermore, as is proved in §4.1, and will be confirmed by DNS, transients will do no more than boost the most unstable eigenmodes in the exponentially unstable flow studied here. Details of the numerical method are given in the Appendix.

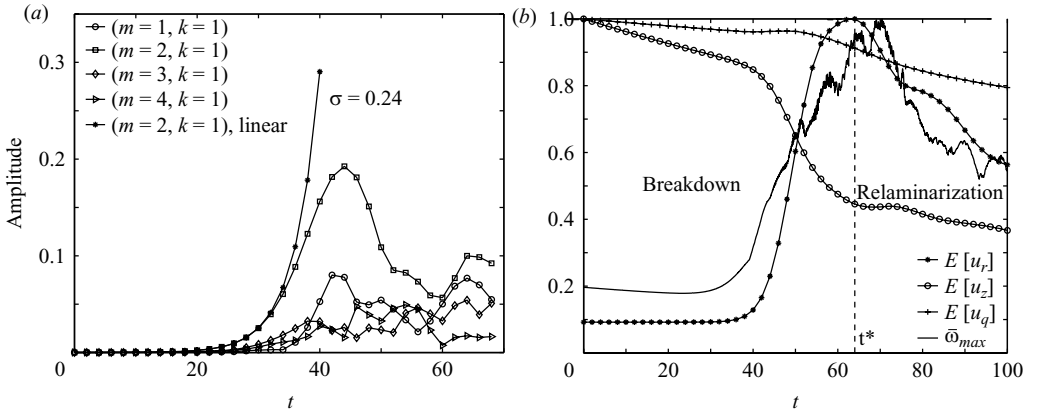

FIGURE 6. (*a*) Plot of the amplitudes, $a_{mk}[\omega_z](r=0.35, t)$, of some unstable DNS modes and comparison with the growth rate, from the linear eigenmode instability theory, of the most unstable mode. (*b*) Plot of energies of the different components of the total velocity field, $\boldsymbol{u}=\boldsymbol{v}+\boldsymbol{V}$, versus time. The maximum norm value, $\bar{\omega}_{max}$, of the total vorticity, $\bar{\boldsymbol{\omega}}=\boldsymbol{\omega}+\boldsymbol{\Omega}$, is also plotted. Note that t_* is greater than the time of validity of the linear instability. (*a*, *b*) $q=-0.4$.

Let us define the amplitude of an (m, k) direct numerical simulation (DNS) mode associated with a perturbation field f, computed using (5.1), as:

$$a_{mk}[f](r,t)=\left|\frac{1}{2\pi L_z}\int_0^{L_z}\int_0^{2\pi} \mathrm{d}\theta\,\mathrm{d}z f(r,\theta,z,t)\exp[-\mathrm{i}(kz+m\theta)]\right|. \tag{5.2}$$

The dependance in (r, t) of this mode is indeed fixed by the nonlinear interactions of perturbations, driven by the Navier–Stokes equations (5.1).

The nonlinear computation procedure is validated by reproducing growth rates of the most unstable eigenmodes given by the linear instability theory, exposed in the previous section. An example of this validation is presented in figure 6(*a*), where the amplitudes $a_{mk}[\omega_z](r=0.35, t)$ are presented for the most significant values of m and k with $q=-0.4$. Clearly the flow is unstable, the different DNS modes grow and the most unstable one has a growth rate, $\sigma=0.24$, in agreement with linear instability predictions. The linear evolution is valid untill $t\simeq 32$; afterwards nonlinear interactions of the different DNS modes become important and the linear instability saturates. This scenario is checked for different values of r and for $q=-0.8$ and $q=-1$.

It is shown in Abid & Brachet (1998), and recalled here in figure 6(*b*), that the nonlinear evolution of the BqV flow could be described, globally, by two phases. In the first one, there is a deceleration and exchange of the kinetic energy from the axial (essentially) and azimuthal velocity components to the radial one (initially not present) by incompressibility. This leads to a drastic change of the initial vortex shape (a breakdown) and intensification of the total vorticity $\bar{\boldsymbol{\omega}}=\boldsymbol{\omega}+\boldsymbol{\Omega}$. The radial velocity reaches a maximum at $t=t_*$; subsequently, the second phase starts, characterized by a decrease of all the quantities and the flow relaminarizes. Note that t_* is greater than the time of validity of the linear theory. A natural question is: does the linearly most unstable eigenmode dominate in the nonlinear regime? In which case it is termed selected in the present work. What about optimal perturbations, with the algebraic growth and transient effects, in the exponentially unstable flow considered herein?

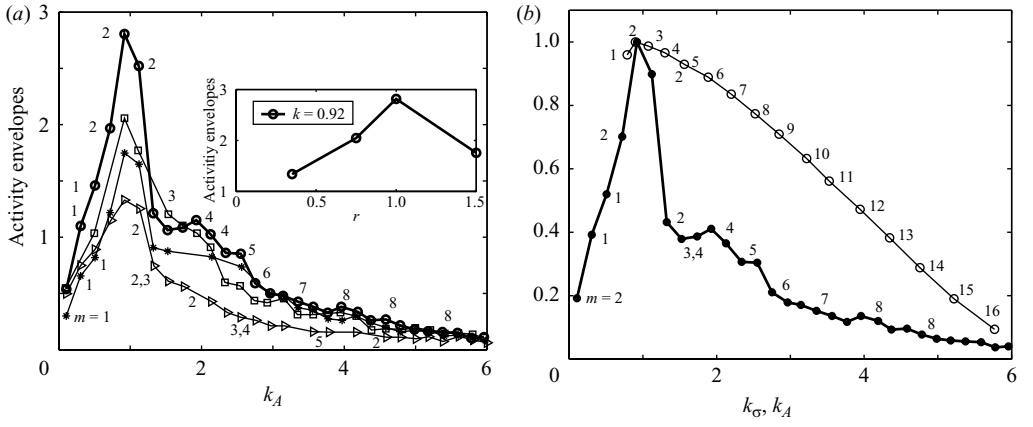

FIGURE 7. (*a*) Plots of activity envelopes, for different r, versus k_A where the activity is maximum at a given m. Notice that the envelopes have an absolute maximum at $m = 2, k = 0.92$ and $r = 1$ (as shown in the inset). △, $r = 0.35$; □, 0.75; ●, 1.0; ∗, 1.5. (*b*) Superposition of the normalized activity envelope, at $r = 1$, and the normalized growth-rate envelope from the linear eigenmode instability theory. The same axis is used for k_A and k_σ and the normalization is chosen such that the maximum of each curve is unity. ○, linear; ● nonlinear. (*a*, *b*) $q = -0.4$.

To address this question, let us define the local activity of an (m, k) DNS mode associated with a perturbation quantity, f, as:

$$A_{mk}[f](r) = \int_0^{t_*} \mathrm{d}t a_{mk}[f](r, t). \tag{5.3}$$

In the present study, only the breakdown regime, $t \leqslant t_*$, is addressed. The relaminarization regime is left for a future work. Similarly to what was done in the previous section, for the growth rate envelope, let us also define the local (at a fixed r) activity envelope: $A_{max} = \max_k A_{mk}[f](r)$, and $k_A(m)$ (or simply k_A), where this maximum occurs. At a given swirl number, q, a DNS mode (m, k) will be termed nonlinearly globally selected (in the mean sense) if the envelopes have an absolute maximum (as a function of k_A), for all r, there. It will be called nonlinearly locally selected if some envelopes have an absolute maximum there, but only around r. A value of r where the activity has an absolute maximum, as a function of r, will be r_A. It is found that all the computed fields have the same behaviour, regarding their activities, in the nonlinear regime. Therefore, only $f = \omega_x$ will be used to show the results. The maximum value of ω_x will be ω_{max}.

For $q = -0.4$, the envelopes are presented in figure 7(*a*) for the most significant values of r (those giving the essential envelope features). Clearly, there is a global selection here: the DNS mode $(m = 2, k = 0.92)$ is an absolute maximum of the envelopes for all r. This DNS mode is selected in a good agreement with the most unstable eigenmode of the linear theory, as shown in figure 7(*b*), where the envelope with the maximum activity is superposed on the exponential growth rate envelope from the linear theory. Note the super-damping of the modes with $m \geqslant 8$ as expected from the shear diffusion mechanism and figure 4(*d*), which shows where this mechanism is most likely to act. According to Bernoff & Lingevitch (1994) a perturbation in a Lamb vortex undergoes damping by a factor $O(\exp[-Re^{-1}m^2(D\Omega)^2t^3/3])$, exhibiting a shear diffusion mechanism. In particular, this damping factor is important where the shear is maximum, i.e. for

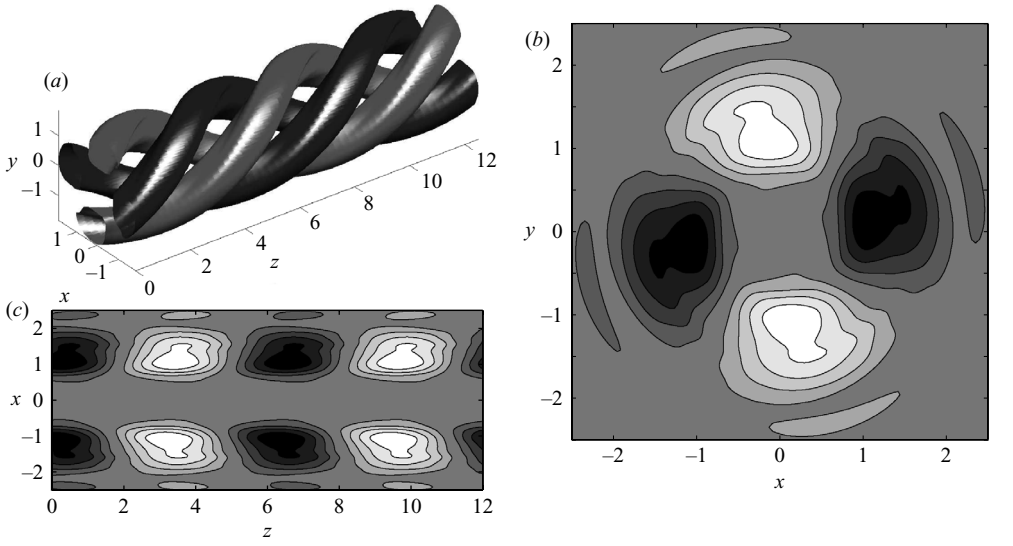

FIGURE 8. Nonlinear DNS mode selection, $q=-0.4$, $m=2$, $k=0.92$, $t=t_*=65$. (a) Isosurfaces of the perturbation vorticity at $\pm 0.5\omega_{max}$. (b) Contour plot of the perturbation vorticity from $-\omega_{max}$ (in black) to $+\omega_{max}$ (in white), at uniform increments, for a fixed z. (c) Same as (b), but at a fixed y.

$r_{D\Omega}=\arg\max_r D\Omega$. For the values of q used in the present work, $r_{D\Omega}\simeq 0.9$. This explains that the perturbations with great values of m (being a vestige of eigenmodes) are super-damped in the nonlinear regime: a damping due to their location near $r_{D\Omega}$ (see figure 4d) enhanced by the m^2 term in the damping factor.

The selected DNS mode here is a quadrupole (four helices). These helices are born near $r=r_e=0.6$ as predicted also from the linear theory (figure 4d). With their mutual induced velocity, they leave the vortex axis and go to its periphery where they spent the most time and cannot survive to the shear diffusion mechanism for $r>1$ since the envelope activities decrease for those values of r as shown in figure 7(a, inset): i.e. $r_A=1\simeq r_{D\Omega}$. So, the essential feature of nonlinearity here is a migration of the helices by their induced velocity. These helices are shown, at $t=t_*$ in figure 8. It is possible to define an angle in the plane $(\boldsymbol{e}_\theta, \boldsymbol{e}_z)$ located at r_λ and corresponding to the maximum basic flow strain rate:

$$\tan(\Phi_\lambda^\nu)=-\frac{1}{r_\lambda}\frac{m}{k_A},$$

as done in the previous sections. It is found that $\Phi_\lambda^\nu=0.8(\pi/2)$ which is exactly the value obtained using the linear eigenmode instability theory. Therefore, it could also be related to the property of alignment of the equiphase angle with the projection of the strain rate eigenvector of the BqV flow (with the maximum eigenvalue) in the plane $(\boldsymbol{e}_\theta, \boldsymbol{e}_z)$.

When $q=-0.8$, the scenario is different and there is no globally selected DNS mode as shown in figure 9(a). However, there are three locally selected modes: $(m=1, k=0.5)$ with an equiphase angle $\Phi_\lambda^\nu\simeq -0.77(\pi/2)$, $[(m=3, k=1.94), \Phi_\lambda^\nu\simeq -0.72(\pi/2)]$ and $[(m=4, k=2.14), \Phi_\lambda^\nu\simeq -0.77(\pi/2)]$. The first one (the most active) is selected near $r=r_A=0.35$ and the two others are equally selected near $r=r_A=0.75$. The most active DNS mode is not the most linearly unstable eigen mode as shown in figure 9(b) where envelopes of activities and growth rates are superposed. However,

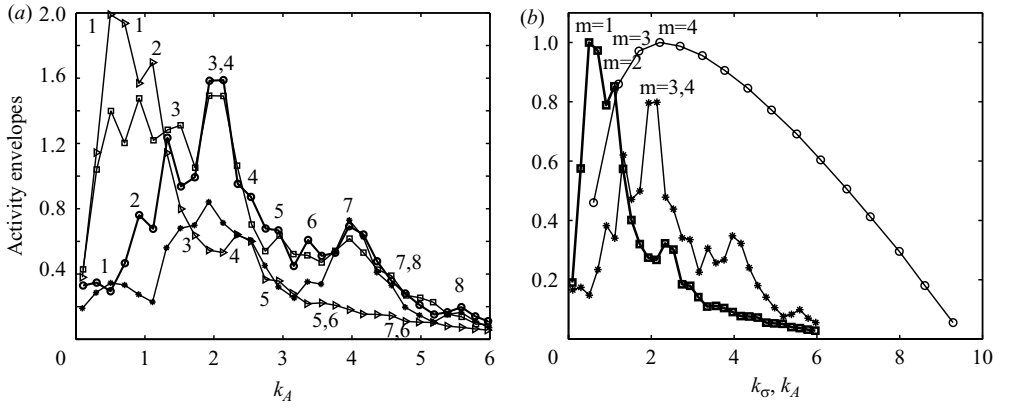

FIGURE 9. (*a*) Plots of activity envelopes, for different r, versus k_A where the activity is maximum at a given m. △, $r=0.35$; □, 0.75; ●, 1.0; ∗, 1.5. There are three locally selected modes: ($m=1, k=0.5$), ($m=3, k=1.94$) and ($m=4, k=2.14$). (*b*) Superposition of the normalized activity envelopes at $r=0.35, 1$ and the normalized growth rate envelope from the linear eigenmode instability theory. The same axis is used for k_A and k_σ and the normalization is chosen such that the maximum of each curve is unity. ○, linear; ∗, nonlinear, $r=1$; ■, nonlinear $r=0.35$. $q=-0.8$.

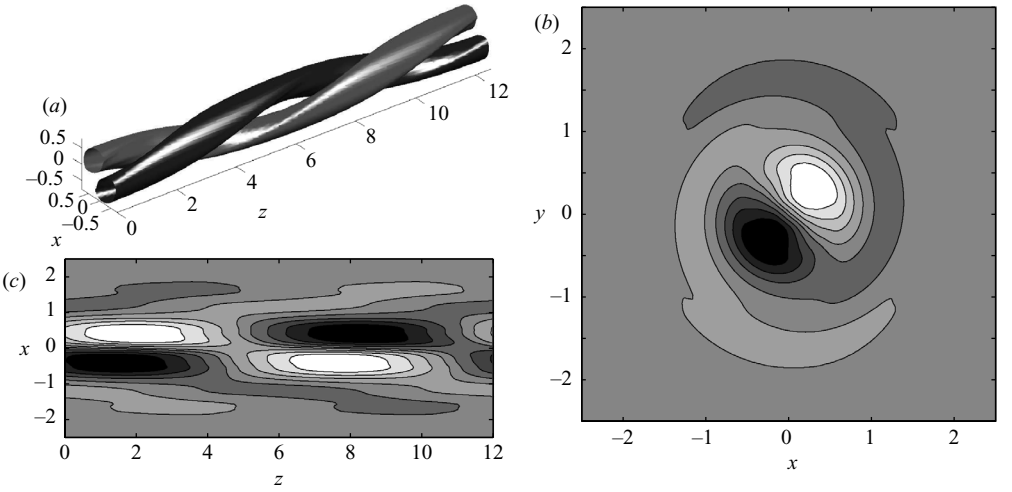

FIGURE 10. Nonlinear DNS mode selection, $q=-0.8$, $m=1$, $k=0.5$, $t=t_*=50$. (*a*) Isosurfaces of the perturbation vorticity at $\pm 0.5\omega_{max}$. (*b*) Contour plot of the perturbation vorticity from $-\omega_{max}$ (in black) to $+\omega_{max}$ (in white), at uniform increments, for a fixed z. (*c*) Same as (*b*), but at a fixed y.

its location, its wavenumber and its equiphase angle could be predicted from the linear theory, i.e. $r_A \simeq r_e$ (from figure 4*d*), $k=k_A=k_\sigma$ (from figure 9*b*) and $\Phi_\lambda^v \simeq \tilde{\Phi}_\lambda^v$. Notice that the modes with $m \geqslant 8$ are also super-damped as could be expected from figure 4(*d*) and the shear diffusion mechanism. The three selected DNS modes, that are scarcely described, are shown in figures 10, 11 and 12.

When $q=-1$, a similar scenario occurs. However, here the most unstable eigenmode from the linear theory is the most active one, and there are two DNS modes locally

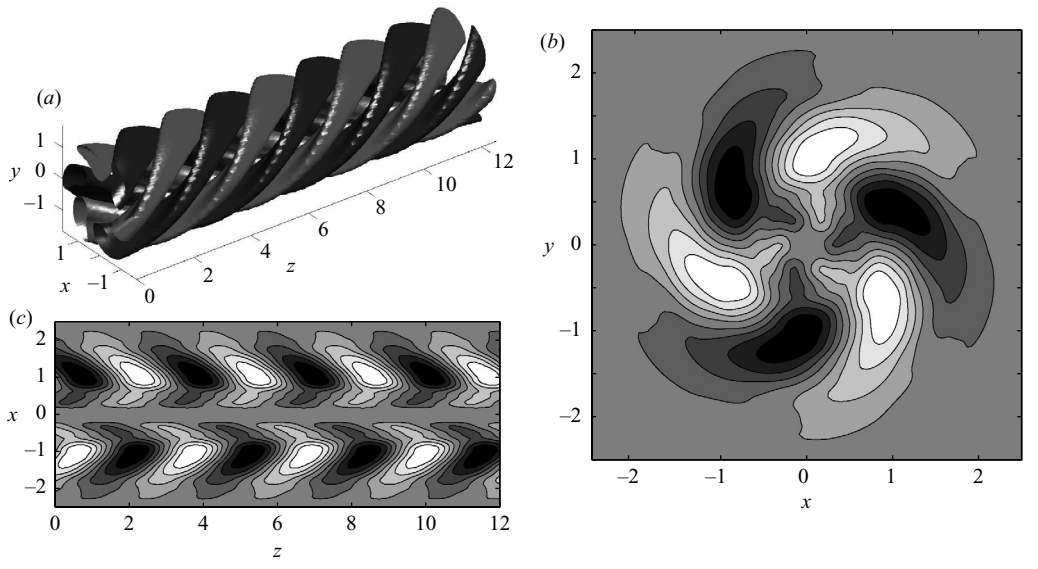

FIGURE 11. Same as figure 10, but $m = 3$, $k = 1.94$.

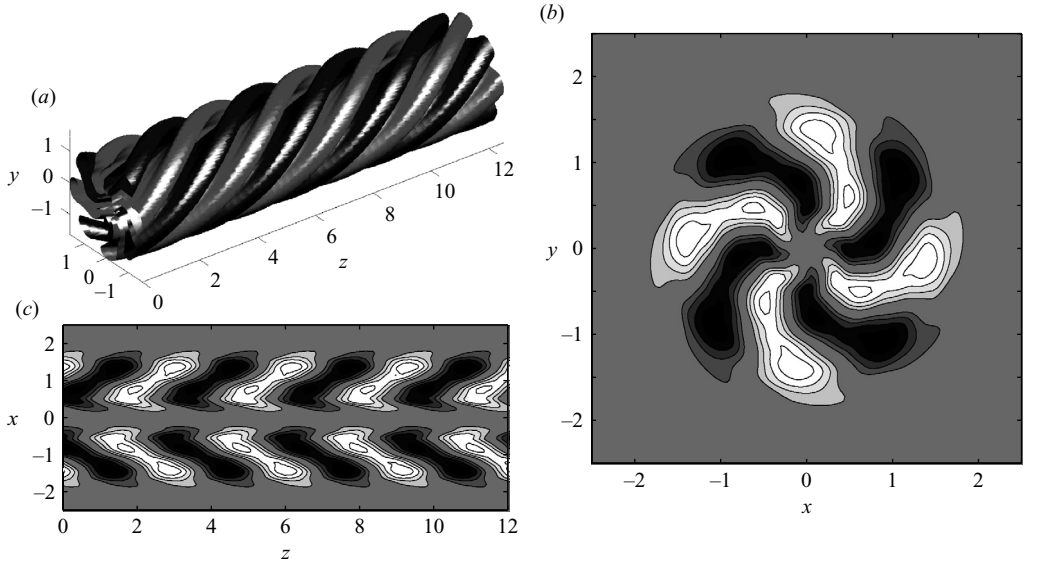

FIGURE 12. Same as figure 10, but $m = 4$, $k = 2.14$.

selected: $[(m = 2, k = 0.91), \Phi_\lambda^v \simeq -0.78(\pi/2)]$ and $[(m = 4, k = 2.54), \Phi_\lambda^v \simeq -0.7(\pi/2)]$ (the most active one) as shown in figure 13. These modes are presented in figures 14 and 15.

Note that the starting time of the relaminarization process, t_*, is diminished when q is increased. It is found that $t_* = 65$ for $q = -0.4$ and $t_* = 50$ for $q = -0.8$ and $q = -1$. On the one hand, it takes much more time for the selected DNS mode, that born nearer to the vortex axis when $q = -0.4$, to reach the periphery of the vortex

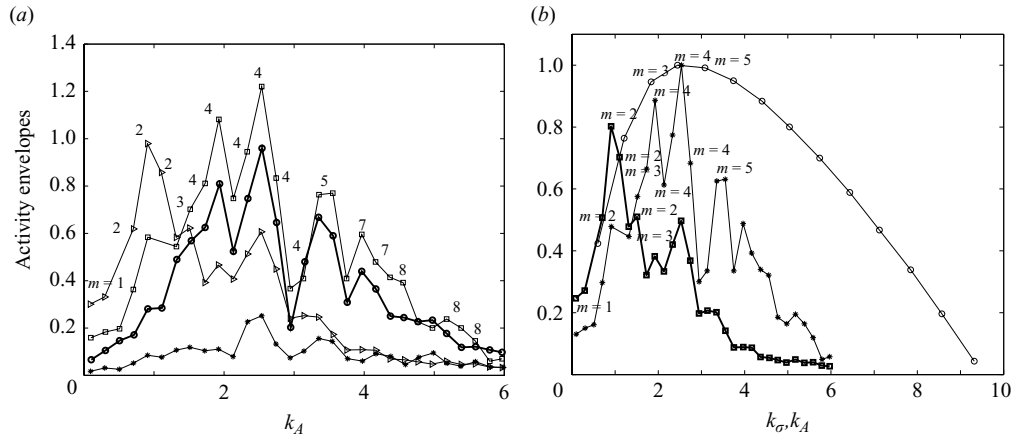

FIGURE 13. (*a*) Plots of activity envelopes, for different r, versus k_A where the activity is maximum at a given m. △, $r = 0.35$; □, 0.75; ●, 1.0; ∗, 1.5. There are two locally selected modes: $(m = 2, k = 0.91)$ and $(m = 4, k = 2.54)$. (*b*) Superposition of the normalized activity envelopes at $r = 0.35$ (■), 0.75 (∗) and the normalized growth-rate envelope from the linear eigenmode instability theory (○). The same axis is used for k_A and k_σ and the normalization is chosen such that the maximum of each curve is unity. (a, b) $q = -1$.

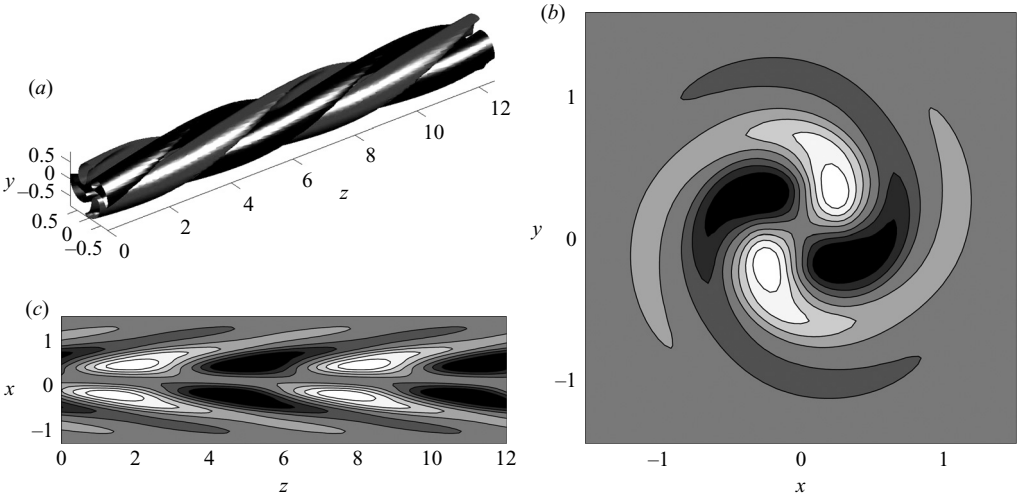

FIGURE 14. Nonlinear DNS mode selection, $q = -1$, $m = 2$, $k = 0.91$, $t = t_* = 50$. (*a*) Isosurfaces of the perturbation vorticity at $\pm 0.5\omega_{max}$. (*b*) Contour plot of the perturbation vorticity from $-\omega_{max}$ (in black) to $+\omega_{max}$ (in white), at uniform increments, for a fixed z. (*c*) Same as (*b*), but at a fixed y.

(where the shear diffusion mechanism becomes significant) than the selected DNS modes for the two other values of the swirl number (see figure 4*d*). On the other hand, the shear, $D\Omega$, increases and the selected modes have greater values of m^2 when q is augmented.

To explain the discrepancy between the nonlinear evolution and the linear eigenmode theory, near the vortex axis, let us consider the possibility of transient

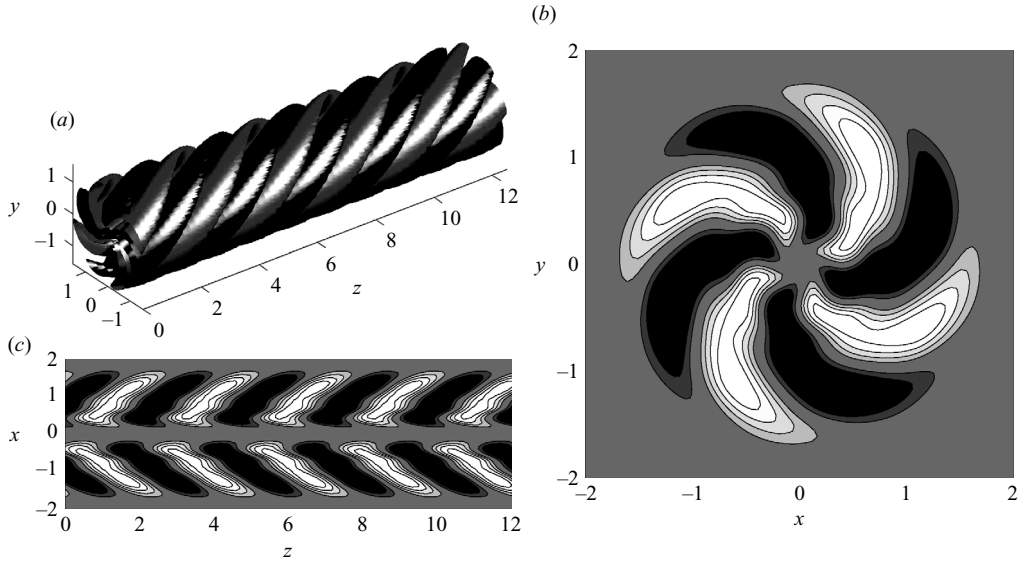

FIGURE 15. Same as figure 14, but $m=4$ and $k=2.54$.

growth of the perturbations since, as shown in § 4.1, $\sqrt{G(t)} \geqslant \mathrm{e}^{\sigma_{max} t}$ in general. For each helical velocity perturbation $\boldsymbol{v}(\boldsymbol{x}, t) = \hat{\boldsymbol{v}}(r, t)\exp[\mathrm{i}(kz+m\theta)]$, solution of the linear initial-value problem (4.1), the maximum energy gain is

$$G(m, k, t) = \max_{\hat{\boldsymbol{v}}_0 \neq \boldsymbol{0}} \frac{||\hat{\boldsymbol{v}}(r, t)\exp[\mathrm{i}(kz + m\theta)]||^2}{||\hat{\boldsymbol{v}}_0||^2}, \tag{5.4}$$

where $\hat{\boldsymbol{v}}_0 \equiv \hat{\boldsymbol{v}}(r, 0)$. The norm used in the $L^2(\mathfrak{D})$ Hilbert space is an integral over the fluid domain and G is indeed a global quantity, i.e. independent of position. Let us define the amplitude gain of the axial vorticity of a DNS mode as

$$a_G(m, k, r, t) = \frac{a_{mk}[\omega_x](r, t)}{a_{mk}[\omega_x](r, 0)}. \tag{5.5}$$

Note that the vorticity is linearly related to the velocity by definition ($\boldsymbol{\omega} = \boldsymbol{\nabla} \times \boldsymbol{v}$). Note also that a gain in a norm of a vector is equal to the gain of its components ($\sqrt{G}||\hat{\boldsymbol{v}}_0|| = ||\sqrt{G}\hat{\boldsymbol{v}}_0||$). Therefore, a_G could be compared to $\sqrt{G}$ without ambiguity in the linear regime.

The amplitude gain as a function of time, obtained by a DNS of the linearized Navier–Stokes equations ((5.1) without $\boldsymbol{v} \times \boldsymbol{\omega}$), is shown in figure 16(*a*) for $q = -0.8$, $m=1$, $k=0.5$ and $r=0.35$ (where the above mentioned discrepancy is substantial). The square root of the energy gain, $\sqrt{G}$ for the same values of q, m and k (kindly given by C. Heaton and obtained by an optimization procedure, see Heaton & Peake 2007), is also plotted for comparison. The maximum exponential growth $\exp(\sigma_{max}(m)t)$ is also shown. Clearly, the DNS mode ($m=1$, $k=0.5$) is subject to a transient growth: $a_G(m, k, r, t) = \sqrt{G(m, k, t)} > \exp(\sigma_{max}(m)t)$. The amplitude gain is greater than that obtained for the eigenmode, but the growth rate has that of the eigenmode as an asymptote, in agreement with (4.13) giving the lower and upper bounds of the gain in general. Therefore, the transient growth boosts the eigenmode ($m=1$) having the maximum exponential growth in the linear regime. Transient growth is unable to

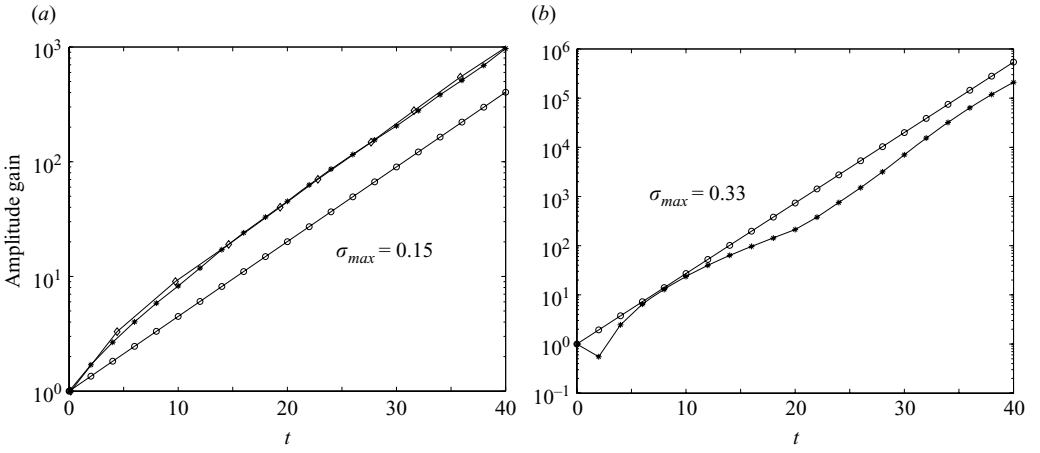

FIGURE 16. Amplitude gain as a function of time obtained by a DNS of the linearized Navier–Stokes equations. (*a*) Transient growth of the $(m = 1, k = 0.5)$ perturbation boosts the eigenmode with the maximum exponential growth in the linear evolution. *, linear DNS, $r = 0.35$; ○, linear eigenmode. The amplitude gain is greater than that obtained for the eigenmode, but the growth rate has that of the eigenmode as an asymptote. The square root of the energy gain, $G^{1/2}$ (◇), is also plotted for comparison. (*b*) Transient growth is unable to produce the same boost for the $(m = 4, k = 2.14)$ case. *, linear DNS; ○, linear eigenmode (a, b) $q = 0.8$.

produce the same boost for the $(m = 4, k = 2.14)$ case as shown in figure 16(*b*) since $a_G(m, k, r, t) \leqslant \exp(\sigma_{max}(m)t)$.

The amplitude gain as a function of time in the nonlinear evolution is shown in figure 17(a, b). Clearly, the transient growth is able to trigger nonlinearities: nonlinearities are triggered before the saturation of the eigenmode $(m = 4, k = 2.14)$ having the absolute maximum exponential growth: $\sigma_{max} = \max_m \sigma_{max}(m)$. In figure 17(*c*), the amplitude, a_{mk}, is plotted as a function of time. Note that the $(m = 1, k = 0.5)$ DNS mode largely dominates, in the nonlinear regime, the DNS mode $(m = 4, k = 2.14)$ that coincides with the eigenmode having the absolute maximum exponential growth in the linear regime. Note also that the latter DNS mode saturates before the former. Therefore, the $(m = 1, k = 0.5)$ DNS mode is nonlinearly selected as the most locally active mode. Let us designate the case $(m = 1, k = 0.5)$ as 'long-wave', and the case $(m = 4, k = 2.14)$ as 'short-wave'. Owing to transient effects, the long-wave component experiences a first boost, in the linear regime, and triggers nonlinearities. However, this initial boost is not sufficient and the selection is due to a second boost in the nonlinear regime: the amplitude of the long-wave component is smaller than the short-wave one (in the nonlinear regime) until the onset of the second boost; after which the state is reversed and the long-wave largely dominates (as shown in figure 17*c*). The situation is very different for the short-wave component: the effect of nonlinearity is simply a saturation (as shown in figure 17*b*). It was checked that the same scenario holds for $q = -1$, and $(m = 2, k = 0.92)$.

Following Heaton & Peake (2007), if we expect that the mechanism for transient growth is inviscid in nature, let us define

$$\Lambda(r, k, \omega) = -\omega + \frac{m}{r} V(r) + kW(r),$$

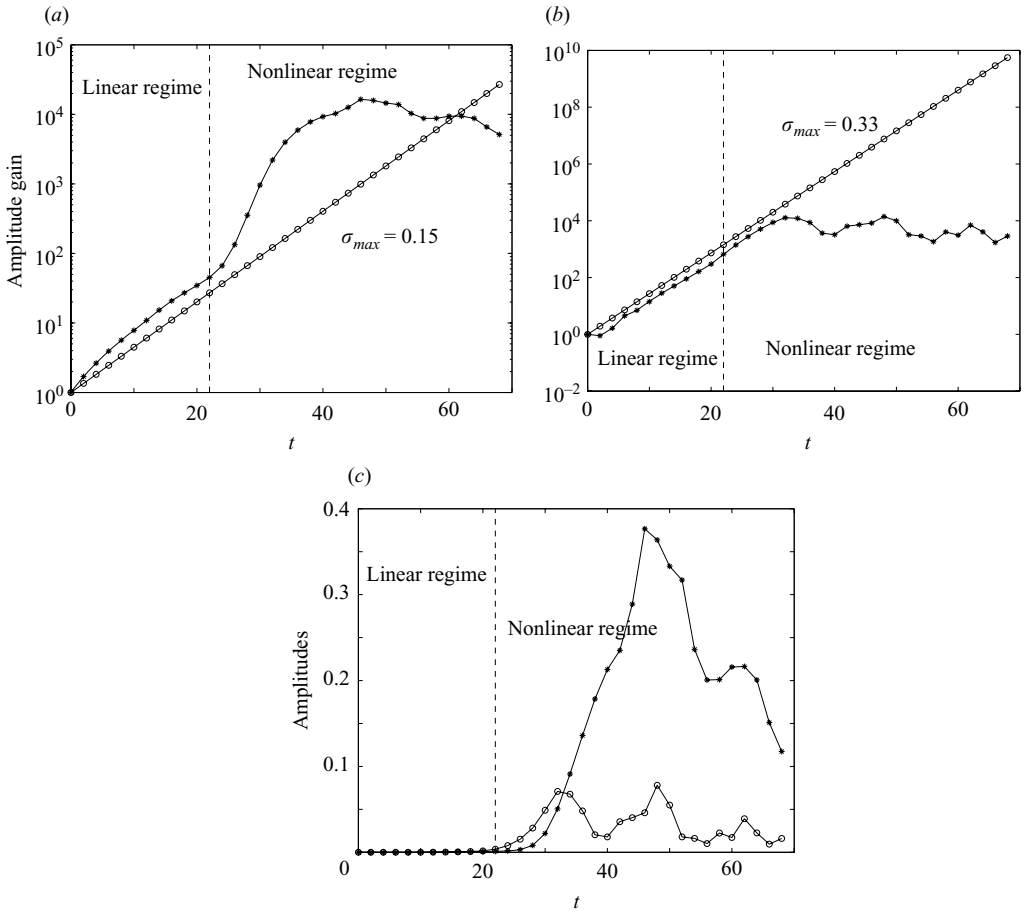

FIGURE 17. (a, b) Amplitude gain as a function of time in the nonlinear evolution. (a) $k = 0.5$, $m = 1$; (b) 2.14, 4. Transient growth is able to trigger nonlinearities: nonlinearities are triggered before the saturation of the eigenmode $(m = 4, k = 2.14)$ having the absolute maximum exponential growth. $*$, nonlinear; $\circ$, linear. (c) Amplitude as a function of time. Note that the $(m = 1, k = 0.5\,(*))$ DNS mode largely dominates, in the nonlinear regime, the DNS mode $(m = 4, k = 2.14(\circ))$ that coincides with the eigenmode having the absolute maximum exponential growth in the linear regime. Note also that the $(m = 1, k = 0.5)$ DNS mode is nonlinearly selected as the most locally active mode owing to a nonlinear boost. $(a$–$c)$ $r = 0.35$.

corresponding to the Lagrangian derivative operator $D_0/Dt \equiv \partial/\partial t + \boldsymbol{V} \cdot \boldsymbol{\nabla}$. Then each frequency of the continuous spectrum

$$\omega_c(r) = \frac{m}{r} V(r) + kW(r), \tag{5.6}$$

contributes to the solution of an initial-value problem, for the perturbation, such that it is approximately convected by the local basic (mean) flow. Indeed, since $\Lambda(r, k, \omega_c(r)) = 0$, ω_c is the frequency corresponding to a pure convection of the unsteady perturbation by the basic flow at radius r. Therefore, using the behaviour of the linearized Euler equations near the critical points, defined by the solutions of (5.6) in r, and the Green function of the linear problem, it can be shown (Heaton & Peake 2006) that the contribution of the continuous spectrum is an algebraic growth

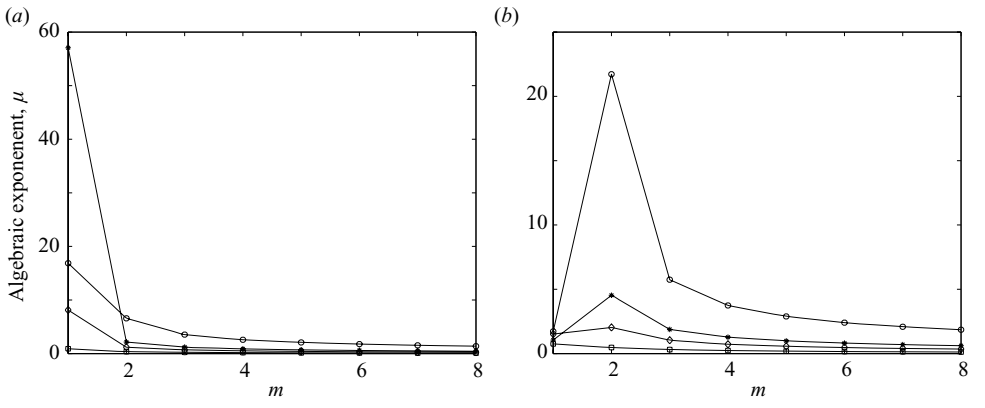

FIGURE 18. Plot of the algebraic growth exponent μ, from the inviscid theory, as a function of m. (*a*) ($k=0.5, q=-0.8$). (*b*) ($k=0.91, q=-1$). Note that the values of $m=(1,2)$, with the maximum algebraic growth, are those of the DNS modes selected in the nonlinear regime near the vortex axis. ○, $r=0.35$; ∗, 0.75; ◇, 1.0; □, 1.5.

of the perturbation. Specifically, $||\boldsymbol{v}|| \sim t^{\mu(r)}$ as $t \to \infty$ where:

$$\mu(r) = Re\left(-\frac{1}{2} + \sqrt{\frac{1}{4} - A(r)}\right),$$

$$A(r) = \frac{2Vk(kD(Vr) - mDW)}{r^2(D\omega_c)^2}.$$

The algebraic growth exponent, μ, is plotted as a function of m in figure 18. For $q=-0.8$ and $k=0.5$, The value of m with the maximum algebraic growth is $m=1$ for all r. It is precisely the DNS mode ($m=1, k=0.5$) that dominates, in the nonlinear regime, the DNS mode ($m=4, k=2.15$) corresponding to the (global) eigenmode with the absolute maximum exponential growth in the linear regime. The same scenario is found for $q=-1$ (figure 18*b*): the value of m with the maximum algebraic growth is $m=2$ in the limit $r \to 0$. Hence, the transient growth observed in these simulations is related to contributions from the inviscid continuous spectrum that persist for the finite, but sufficiently high, Reynolds number used here.

6. Conclusion

Fully nonlinear mode selection in the Batchelor trailing line q vortex flow, in the breakdown regime and for $Re=1000$, is presented. It is shown that nonlinear effects become significant when the swirl intensity increases. Furthermore, nonlinear effects are confined near the vortex axis. Far from the axis, linear exponential instability theory provides a good guess at the dynamics in the nonlinear regime. More precisely, for a low swirl number, ($|q|=0.4$), a four helix DNS mode (($m=2, k=0.92$), a quadrupole) is selected in agreement with the most unstable eigenmode perturbation from the linear instability theory. This quadrupole helix is located near the initial vortex core radius and has an equiphase angle, $\Phi_\lambda^v \simeq -0.8(\pi/2)$, that could be predicted both from the energy equation and from the linear eigenmode theory. When the swirl number is increased ($|q|=0.8$ or 1), nonlinear effects manifest themselves, essentially, by long-wave mode generation near the vortex axis. These DNS modes are ($m=1, k=0.5$) with an equiphase angle $\Phi_\lambda^v \simeq -0.77(\pi/2)$

for $|q|=0.8$, and $(m=2, k=0.91)$, $\Phi_\lambda^v \simeq -0.78(\pi/2)$ for $|q|=1$. Far from the vortex axis, and near the initial vortex core radius, the most active modes are: $[(m=3, k=1.94), \Phi_\lambda^v \simeq -0.72(\pi/2)]$ and $[(m=4, k=2.14), \Phi_\lambda^v \simeq -0.77(\pi/2)]$ for $|q|=0.8$, and $[(m=4, k=2.54), \Phi_\lambda^v \simeq -0.7(\pi/2)]$ for $|q|=1$. These last modes are selected in good agreement with the most unstable eigenmodes from the linear instability theory and also from the energy perturbation equation.

The discrepancy between the nonlinear evolution and the linear eigenmode theory is related to the transient growth of optimal perturbations resulting from the non-normality of the linearized Navier–Stokes equations about shear flows. It is shown that the algebraic (transient) growth contributions from the inviscid continuous spectrum could trigger nonlinearities near the flow axis. The DNS mode selected in the nonlinear regime coincides with the long-wave eigenmode benefiting from the algebraic growth in the linear regime. This eigenmode is different from the short-wave eigenmode with the absolute maximum exponential growth. Although it is promoted by transients, in the linear regime, the long-wave component is selected nonlinearly.

These findings raise the question of the interaction of helical vortices as a fundamental problem in the understanding of vortex breakdown and eventually some aspects of turbulence and its small scales. The selected DNS modes in the nonlinear breakdown phase are vestiges of helical eigenmodes. Furthermore, it is shown in an experiment on vortex filaments in turbulence, by Cadot, Douady & Couder (1995), that these filaments are subject to helical breakdown leading to small scales as thin as the Kolmogorov scale. Finally, the extensions of the present work in the relaminarization regime and for $|q|>1.6$, where viscous modes are in action, are straightforward in principle and are left for a future work.

The author would like to acknowledge an anonymous referee for pointing out the possibility of a transient growth of the perturbations to explain the discrepancy between the nonlinear evolution and the linear eigenmode theory.

C. Heaton is acknowledged for providing the optimal perturbation gain of figure 16.

Fruitful discussions with S. Le Dizès are acknowledged. The administration (as a wizard) of the CLUSTER at IRPHE by L. Raymond, and his patience, are also acknowledged. This work was supported by the 'Agence Nationale pour la recherhe' under contract: ANR vortex.

Appendix. Numerical method

Let $\boldsymbol{u}=\boldsymbol{v}+\boldsymbol{V}=(u, v, w)$ be the total velocity and $\bar{\boldsymbol{\omega}}=\nabla\times\boldsymbol{u}$ the total vorticity. Therefore equations (5.1) are simply the standard Navier–Stokes equations:

$$\frac{\partial \boldsymbol{u}}{\partial t}=\boldsymbol{u}\times\bar{\boldsymbol{\omega}}-\nabla\bar{\Pi}+\nu\Delta\boldsymbol{u}\ , \tag{A 1}$$

$$\nabla\cdot\boldsymbol{u}=0\ , \tag{A 2}$$

where $\bar{\Pi}=\bar{p}+u^2/2$ and $\bar{p}$ is the total fluid pressure. Therefore, with periodic boundary conditions, the conservation of energy equation is (using the summation over repeated indices):

$$\frac{\mathrm{d}E[\boldsymbol{u}]}{\mathrm{d}t}=\frac{\mathrm{d}}{\mathrm{d}t}\int_{\mathfrak{D}}\mathrm{d}\boldsymbol{x}\,\frac{u_k^2}{2}=-\frac{\nu}{2}\int_{\mathfrak{D}}\mathrm{d}\boldsymbol{x}\,(\partial_i u_k+\partial_k u_i)^2. \tag{A 3}$$

For an inviscid fluid, $\nu=0$, and the total energy E is constant. This motivated the use of rotational formulation.

Application of (A 2) to (A 1) leads to:

$$\Delta\bar{\Pi} = \nabla\cdot(\boldsymbol{u}\times\bar{\boldsymbol{\omega}})\ . \tag{A 4}$$

This equation could be written symbolically:

$$\bar{\Pi} = (\Delta)^{-1}\nabla\cdot(\boldsymbol{u}\times\bar{\boldsymbol{\omega}})\ , \tag{A 5}$$

where $(\Delta)^{-1}$ is the inverse of Laplace operator that is defined, without ambiguity, using the Fredholm alternative of orthogonality to the kernel space of the adjoint operator to be inverted. Therefore, the problem given by (A 1) and (A 2) could be recast to the resolution of only one equation:

$$\frac{\partial\boldsymbol{u}}{\partial t} = (1-\nabla(\Delta)^{-1}\nabla\cdot)\boldsymbol{u}\times\bar{\boldsymbol{\omega}} + \nu\Delta\boldsymbol{u}. \tag{A 6}$$

This is simply the method of projection on the divergence-free vector space (Peyret 2002). With periodic boundary conditions, the NS equations are actually solved for a periodic array of swirling vortices. As the behaviour of only one vortex is under consideration, the planes $x = nL_x$, $y = pL_y$ (n and p integers; L_x and $L_y \gg 1$) are used as reflection planes by real sine or cosine Fourier transforms. The axial direction of the vortex is free and complex Fourier transforms are used (see figure 20).

Therefore, any three-dimensional scalar field, Ψ, is written in the following form:

$$\Psi(\boldsymbol{x},t) = \sum_{k_x,k_y,k_z} \hat{\Psi}(\boldsymbol{k},t)\mathrm{e}^{\mathrm{i}k_z z_k} \begin{pmatrix}\cos(k_x x_i)\\ \text{or}\\ \sin(k_x x_i)\end{pmatrix} \begin{pmatrix}\cos(k_y y_j)\\ \text{or}\\ \sin(k_y y_j)\end{pmatrix}. \tag{A 7}$$

The inverse transform is given by:

$$\hat{\Psi}(\boldsymbol{k},t) = \sum_{i,j,k} \frac{c_{ij}}{N_x N_y N_z}\Psi(\boldsymbol{x},t)\mathrm{e}^{-\mathrm{i}k_z z_k} \begin{pmatrix}\cos(k_x x_i)\\ \text{or}\\ \sin(k_x x_i)\end{pmatrix} \begin{pmatrix}\cos(k_y y_j)\\ \text{or}\\ \sin(k_y y_j)\end{pmatrix}, \tag{A 8}$$

where,

$$\boldsymbol{x} = (x_i, y_j, z_k),$$
$$\boldsymbol{k} = (k_x, k_y, k_z) = (k_1, k_2, k_3),$$
$$k_x \in \frac{2\pi}{L_x}\left[-\frac{N_x}{2}, \frac{N_x}{2}-1\right], \quad k_y \in \frac{2\pi}{L_y}\left[-\frac{N_y}{2}, \frac{N_y}{2}-1\right], \quad k_z \in \frac{2\pi}{L_z}\left[-\frac{N_z}{2}, \frac{N_z}{2}-1\right],$$
$$i \in [0, N_x-1], \quad j \in [0, N_y-1], \quad k \in [0, N_z-1],$$
$$x_i = i\Delta x,\ y_j = j\Delta y,\ z_k = k\Delta z,$$
$$\Delta x = \frac{L_x}{N_x-1},\ \Delta y = \frac{L_y}{N_y-1},\ \Delta z = \frac{L_z}{N_z-1},$$
$$c_{ij} = \tfrac{1}{4} \text{ if } x_i = y_j = 0,\ \tfrac{1}{2} \text{ if } x_i = 0 \text{ or } y_j = 0 \text{ and } 1 \text{ if } x_i \neq 0,\ y_j \neq 0.$$

This spectral representation is four times faster and less memory consuming than a standard complex Fourier transform in three space directions.

Thus, the Fourier transform in z is always complex, but in the lateral directions x and y there are four possibilities summed up in the table 1. In conclusion, there are four possible three-dimensional Fourier transforms that will be denoted simply as $\mathscr{F}$

×	C_x	S_x
C_y	C_xC_y	S_xC_y
S_y	C_xS_y	S_xS_y

TABLE 1. The different possibilities for the lateral Fourier transform: C for a cosine and S for a sine.

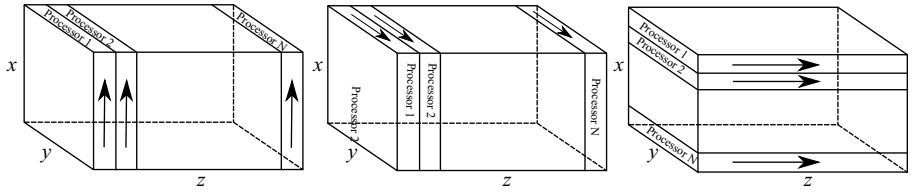

FIGURE 19. Volume parallelization of three-dimensional Fourier transforms. Data are partitioned into N parts according to the number of processors. Arrows show the fast-Fourier-transform directions and consequently the data storage in each case.

(and their inverses $\mathscr{F}^{-1}$) which are one of:

$$\mathscr{F}^{e_z C_x C_y}, \quad \mathscr{F}^{e_z S_x C_y}, \quad \mathscr{F}^{e_z C_x S_y}, \quad \mathscr{F}^{e_z S_x S_y}, \tag{A 9}$$

where e_z is the complex exponential in the z-direction. These transforms are implemented using the fast-Fourier-transform algorithm and parallelized in volume as explained in figure 19.

A.1. *Calculus of* $\mathscr{F}(\nabla)$ *et de* $\mathscr{F}(\Delta)$

It is easy to show that: $\mathscr{F}(\nabla\Psi) = \boldsymbol{k}\mathscr{F}(\Psi)$ with:

$$\left.\begin{array}{lll} \boldsymbol{k} = [-k_x, -k_y, ik_z]^T & \text{if} & \Psi = \sum_{k_x,k_y,k_z} \hat{\Psi} e_z C_x C_y \ , \\ \boldsymbol{k} = [k_x, -k_y, ik_z]^T & \text{if} & \Psi = \sum_{k_x,k_y,k_z} \hat{\Psi} e_z S_x C_y \ , \\ \boldsymbol{k} = [-k_x, k_y, ik_z]^T & \text{if} & \Psi = \sum_{k_x,k_y,k_z} \hat{\Psi} e_z C_x S_y \ , \\ \boldsymbol{k} = [k_x, k_y, ik_z]^T & \text{if} & \Psi = \sum_{k_x,k_y,k_z} \hat{\Psi} e_z S_x S_y, \end{array}\right\} \tag{A 10}$$

and that always:

$$\mathscr{F}(\Delta\Psi) = -\left(k_x^2 + k_y^2 + k_z^2\right)\mathscr{F}(\Psi) = -||\boldsymbol{k}||^2\mathscr{F}(\Psi). \tag{A 11}$$

A.2. *Application to different fields of Navier–Stokes equations*

Figure 20 shows different components of the velocity vector on the boundaries of $\mathfrak{D}$. On these boundaries, each velocity component is constrained by a reflection condition. This gives its dependence in x and y regarding parity: cosine for symmetric component and sine for antisymmetric one. Table 2 sums up spatial dependencies of different fields of NSE.

In the following, all fields are considered to be in spectral space. Using (A 10) and (A 11), equation (A 6) could be written:

$$\frac{\partial u_i}{\partial t} = \sum_j \left(\delta_{ij} - \epsilon_{ij}\frac{k_i k_j}{||\boldsymbol{k}||^2}\right)\left[\mathscr{F}(\mathscr{F}^{-1}(\boldsymbol{u}) \times \mathscr{F}^{-1}(\bar{\boldsymbol{\omega}}))\right]_j - \nu||\boldsymbol{k}||^2 u_i \ , \tag{A 12}$$

Field	x dependence	y dependence	z dependence
u	S_x	C_y	e_z
v	C_x	S_y	e_z
w	C_x	C_y	e_z
u^2	C_x	C_y	e_z
$\bar{\omega}_x$	C_x	S_y	e_z
$\bar{\omega}_y$	S_x	C_y	e_z
$\bar{\omega}_z$	S_x	S_y	e_z
$(\boldsymbol{u} \times \bar{\boldsymbol{\omega}})_x$	S_x	C_y	e_z
$(\boldsymbol{u} \times \bar{\boldsymbol{\omega}})_y$	C_x	S_y	e_z
$(\boldsymbol{u} \times \bar{\boldsymbol{\omega}})_z$	C_x	C_y	e_z
$\bar{p}$	C_x	C_y	e_z

TABLE 2. The different field representations: C for a cosine, S for a sine and e for exponential.

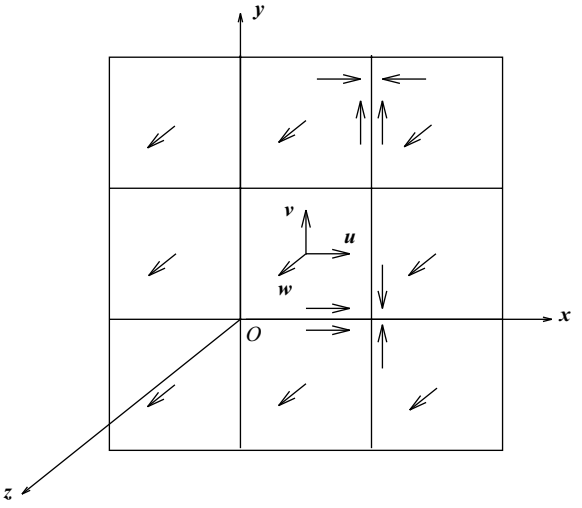

FIGURE 20. Reflections and free slip conditions.

where ϵ_{ij} is given by:

$$[\epsilon_{ij}] = \begin{bmatrix} 1 & 1 & i \\ 1 & 1 & i \\ -i & -i & 1 \end{bmatrix}. \tag{A 13}$$

This equation could be written in a compact form:

$$\frac{\partial \boldsymbol{u}}{\partial t} = \boldsymbol{C} + \boldsymbol{D}, \tag{A 14}$$

where $\boldsymbol{C}$ stands for the nonlinear term and $\boldsymbol{D}$ for the linear diffusive term. This equation is integrated in time using the explicit Adams–Bashforth scheme for the nonlinear part and the implicit Crank–Nicolson scheme for the linear part:

$$\frac{\boldsymbol{u}^{n+1} - \boldsymbol{u}^n}{\Delta t} = \frac{3\boldsymbol{C}^n - \boldsymbol{C}^{n-1}}{2} + \frac{\boldsymbol{D}^{n+1} + \boldsymbol{D}^n}{2}, \tag{A 15}$$

where $\boldsymbol{u}^{n+1} = \boldsymbol{u}(\boldsymbol{x}, t = (n+1)\Delta t)$. Using $\boldsymbol{D} = -\nu k^2 \boldsymbol{u}$, the following discrete evolution equation is obtained for $\boldsymbol{u}^n$:

$$\boldsymbol{u}^{n+1} = \frac{(1 - \nu k^2 \Delta t/2)\boldsymbol{u}^n + (\Delta t/2)(3\boldsymbol{C}^n - \boldsymbol{C}^{n-1})}{(1 + \nu k^2(\Delta t/2))}. \tag{A 16}$$

This scheme is second-order accurate in time. For the first time step, the Euler scheme is used:

$$\boldsymbol{u}^1 = \boldsymbol{u}^0 + \Delta t[\boldsymbol{C}^0 + \boldsymbol{D}^0]. \tag{A 17}$$

The error of this method is globally $O(\Delta t^2)$. The stability of the numerical algorithm is obtained by using a CFL number equal to 0.2 and the spectral convergence is ensured throughout each simulation. Aliasing errors are efficiently eliminated using the Orszag two-thirds rule (Orszag 1971; Canuto *et al.* 1987). The consistency of the overall procedure is checked by reproducing growth rates from the linear instability theory as shown in figure 6 (*a*).

REFERENCES

Abid, M. & Brachet, M. E. 1998 Direct numerical simulations of the Batchelor trailing vortex by a spectral method. *Phys. Fluids* **10**, 469–475.

Antkowiak, A. & Brancher, P. 2004 Transient energy growth for the Lamb–Oseen vortex. *Phys. Fluids* **16**, L1–L4.

Batchelor, G. K. 1964 Axial flow in trailing line vortices. *J. Fluid Mech.* **20**, 645–658.

Bernoff, A. J. & Lingevitch, J. F. 1994 Rapid relaxation of an axisymmetric vortex. *Phys. Fluids* **6**, 3717–3723.

Butler, K. M. & Farrell, B. F. 1992 Three dimensional optimal perturbations in viscous shear flow. *Phys. Fluids* **4**, 1637–1650.

Cadot, O., Douady, S. & Couder, Y. 1995 Characterization of the low-pressure filaments in a three-dimensional turbulent shear flow. *Phys. Fluids* **7**(3), 630–646.

Canuto, C., Hussaini, M., Quarteroni, A. & Zang, T. 1987 *Spectral Methods in Fluid Dynamics*. Springer.

Delbende, I. & Rossi, M. 2005 Nonlinear evolution of a swirling jet instability. *Phys. Fluids* **17**, 1–21.

Delbènde, I., Chomaz, J. & Huerre, P. 1998 Absolute/convective instabilities in the Batchelor vortex: a numerical study of the linear impulse response. *J. Fluid Mech.* **335**, 229–254.

Duck, P. W. & Khorrami, M. R. 1992 A note on the effects of viscosity on the stability of a trailing-line vortex. *J. Fluid Mech.* **245**, 175–189.

Fabre, D. & Jacquin, L. 2004 Viscous instabilities in trailing line vortices at large swirl numbers. *J. Fluid Mech.* **500**, 239–262.

Gallaire, F. & Chomaz, J. M. 2003 Mode selection in swirling jet experiments: a linear stability analysis. *J. Fluid Mech.* **494**, 223–253.

Heaton, C. J. 2007 Centre modes in inviscid swirling flows and their application to the stability of the Batchelor vortex. *J. Fluid Mech.* **576**, 325–348.

Heaton, C. J. & Peake, N. 2006 Algebraic and exponential instability of inviscid swirling flow. *J. Fluid Mech.* **565**, 279–318.

Heaton, C. J. & Peake, N. 2007 Transient growth in vortices with axial flow. *J. Fluid Mech.* **587**, 271–301.

Herrada, M. A. & Fernandez-Feria, R. 2006 On the development of three-dimensional vortex breakdown in cylindrical regions. *Phys. Fluids* **18**, 084105.

Khorrami, M. R. 1991 On the viscous modes of instability of a trailing line vortex. *J. Fluid Mech.* **225**, 197–212.

Landau, L. D. & Lifshitz, E. M. 1987 *Fluid Mechanics*. Pergamon.

Le Dizès, S. & Fabre, D. 2007 Large-Reynolds-number asymptotic analysis of viscous centre modes in vortices. *J. Fluid Mech.* **585**, 153–180.

Leibovich, S. & Stewartson, K. 1983 A sufficient condition for the instability of columnar vortices. *J. Fluid Mech.* **126**, 335–356.

Lessen, M., Singh, P. W. & Paillet, F. 1974 The stability of a trailing line vortex. Part 1. Inviscid theory. *J. Fluid Mech.* **63**, 753–763.

Mayer, E. W. & Powell, K. G. 1992 Viscous and inviscid instabilities of a trailing vortex. *J. Fluid Mech.* **245**, 91–114.

Olendraru, C., Sellier, A., Rossi, M. & Huerre, P. 1996 Absolute/convective instability of the Batchelor vortex. *J. Fluid Mech.* **323**, 153–159.

Orszag, S. A. 1971 On the elimination of aliasing in finite-difference schemes by filtering high-wavenumber componenets. *J. Atmos. Sci.* **28**, 1074–1074.

Peyret, R. 2002 *Spectral Methods for Incompressible Viscous Flow*. Springer.

Pradeep, D. S. & Hussain, F. 2006 Transient growth of perturbation in a vortex column. *J. Fluid Mech.* **550**, 251–288.

Ruith, M. R., Chen, P., Meiburg, E. & Maxworthy, T. 2003 Three dimensional vortex breakdown in swirling jets and wakes: direct numerical simulation. *J. Fluid Mech.* **486**, 331–378.

Satish, C. R. & Henningson, D. S. 1993 Energy growth in viscous channel flows. *J. Fluid Mech.* **252**, 209–238.

Schmid, P. & Henningson, D. 2001 *Stability and Transition in Shear Flows*. Springer.

Schmid, P. J. 2007 Nonmodal stability theory. *Annu. Rev. Fluid Mech.* **39**, 129–162.

Stewartson, K. 1982 The stability of swirling flows at large Reynolds number when subjected to disturbances with large azimuthal wavenumber. *Phys. Fluids* **25**, 1953–1957.

Stewartson, K. & Brown, S. N. 1985 Near-neutral centre-modes as inviscid perturbations to a trailing line vortex. *J. Fluid Mech.* **156**, 387–399.

Stewartson, K. & Leibovich, S. 1987 On the stability of a columnar vortex to disturbances with large azimuthal wavenumber: the lower neutral points. *J. Fluid Mech.* **178**, 549–566.

Trefethen, L. N., Trefethen, A. E., Reddy, S. C. & Driscoll, T. A. 1993 Hydrodynamic stability without eigenvalues. *Science* **261**, 578–584.